minerals

MDPI

Article

Integrated VNIR–SWIR Spectral, Mineralogical, and Geochemical Classification of Hydrothermal Alteration Zones in the Shadan Au–Cu System, Eastern Iran

Niloofar Nayebi [1,*], Davood Raeisi [1,2,*], Hossein Fallahi [3], Shahrouz Babazadeh [2,4] and Soroush Modabberi [1]

[1] School of Geology, College of Science, University of Tehran, Tehran 141556455, Iran; modabberi@ut.ac.ir
[2] Karand Sadr Jahan Mines and Mineral Industries Co., Tehran 1968816619, Iran; shahrouz.babazadeh@gmail.com
[3] Department of Earth Sciences, Faculty of Natural Sciences, University of Tabriz, Tabriz 5166616471, Iran; hosein.falahi@gmail.com
[4] Natural Science Research Institute, Chungnam National University, Daejeon 34134, Republic of Korea
* Correspondence: niloofar_nayebi@ut.ac.ir (N.N.); d.raeisi@ut.ac.ir (D.R.)

Abstract

An integrated Visible–Near-Infrared to Shortwave Infrared spectroscopy (VNIR–SWIR spectral), mineralogical, and geochemical study was conducted on the Shadan Au–Cu porphyry–epithermal system in the eastern Lut Block, Iran, to characterize hydrothermal alteration zonation and classify alteration–lithological units. Thirty-eight representative samples were analyzed by reflectance spectroscopy (0.35–2.50 μm), petrography, XRD (X-ray Diffraction), X-ray fluorescence (XRF), and Inductively Coupled Plasma Mass Spectrometry (ICP–MS). Quantitative continuum-removal processing identified diagnostic absorption features near 0.90, 1.40, 1.90, 2.17, 2.20, 2.33, and 2.50 μm, corresponding to Fe^{3+}, Al–OH, H_2O, and CO_3 absorptions. Seven alteration–lithological groups (G_1–G_7) were defined and verified by XRD and petrography, representing illite–smectic–kaolinite (argillic), alunite–dickite (advanced argillic), quartz–silicified, Fe-oxide, oxidized argillic, chlorite–epidote (propylitic), and carbonate–iron vein assemblages. Whole-rock geochemical data reveal coherent enrichments of Al_2O_3–K_2O in clay-dominant zones, Fe_2O_3 in oxide-rich areas, and CaO–MgO in carbonate-bearing assemblages. Spectral and geochemical integration delineates a vertically and laterally zoned system evolving from acidic to neutral–oxidizing conditions, typical of low-sulfidation epithermal overprints on porphyry-style magmatic centers. This multidisciplinary framework demonstrates the value of combining VNIR–SWIR spectroscopy with mineralogical and geochemical constraints for vectoring and classification of alteration systems in post-collisional volcanic belts.

Keywords: porphyry–epithermal alteration; VNIR–SWIR spectroscopy; hydrothermal mineralogy; geochemical classification; Shadan Au–Cu system

Check for updates

Academic Editor: Bernard Hubbard

Received: 29 December 2025
Revised: 24 February 2026
Accepted: 26 February 2026
Published: 2 April 2026

Copyright: © 2026 by the authors. Licensee MDPI, Basel, Switzerland. This article is an open access article distributed under the terms and conditions of the Creative Commons Attribution (CC BY) license.

1. Introduction

The foundation of Visible–Near-Infrared to Shortwave Infrared spectroscopy (VNIR–SWIR) in geology was established by the seminal works of [1–3], who linked absorption features of Al–OH, Mg/Fe–OH, CO_3 and Fe^{3+} to specific mineral groups. This framework underpins modern spectral libraries such as the USGS Spectral Library [4] and more recent compilations for exploration applications [5,6]. Early airborne hyperspectral mapping using Airborne Visible/Infrared Imaging Spectrometer (AVIRIS) and Hyperspectral Mapper

(HyMap) demonstrated successful delineation of alteration zones in volcanic–plutonic settings [7], especially using diagnostic bands near ~1.40, 1.90, 2.20, 2.30–2.35, ~2.50, and ~0.90 µm. Subsequent spectral mapping in porphyry–epithermal provinces of the Andes, Great Basin, and Tibet showed how argillic, phyllic, silicic, propylitic and carbonate assemblages can be resolved using continuum removal and mineral indices [8–12]. Studies on leached caps and oxidation blankets emphasized the importance of Fe^{3+} bands near 0.85–0.95 µm [13–16].

Recent advances with Environmental Mapping and Analysis Program (EnMAP), PRecursore IperSpettrale della Missione Applicativa (PRISMA), Airborne Visible/Infrared Imaging Spectrometer–Next Generation (AVIRIS-NG) and Hyperspectral Scanner (HySpex) have transformed deposit-scale mineral mapping [16] in which EnMAP is used to resolve illite, chlorite, and epidote in porphyry systems with higher accuracy than multispectral sensors. Some scholars demonstrated PRISMA's ability to discriminate IOCG, epithermal, and porphyry alteration fronts with greater fidelity than Advanced Spaceborne Thermal Emission and Reflection Radiometer (ASTER) [17,18]. New work with AVIRIS-NG and HySpex confirms the value of integrating spectra with X-ray Diffraction (XRD), thin sections, Inductively Coupled Plasma Mass Spectrometry (ICP-MS) geochemistry and field validation [14]. Additional developments in spectral-feature extraction and AI-based mineral prediction are now emerging for exploration [19]. Collectively, classic and modern studies confirm that VNIR–SWIR absorption features reliably trace mineral chemistry, fluid–rock processes, and hydrothermal zonation. Their integration with petrography, XRD and lithogeochemistry justifies the Shadan approach and supports the classification of seven spectral–lithological groups that mirror global epithermal–porphyry alteration trends.

Eastern Iran comprises two major geological domains: the Lut Block and the Sistan suture zone. The Lut Block forms the eastern part of the Central Iranian Microcontinent and hosts numerous porphyry–epithermal systems (Figure 1). It extends roughly 900 × 200 km and is bounded by the Sistan suture and Nehbandan Fault to the east, the Nayband Fault and Shotori Range to the west (separating it from the Tabas Block), and the Great Kavir (Dorouneh) Fault to the north (Figure 2). The Sistan suture zone, ~700 km long, represents the Cretaceous closure of the Sistan Ocean, a branch of the Neotethys, following subduction beneath the Afghan Block and subsequent collision with the Lut Block in the Late Cretaceous [20]. It comprises an accretionary complex of oceanic fragments (ophiolites), high-pressure metamorphic rocks (blueschists and eclogites), and deep-marine sediments such as radiolarites, limestones, and turbidites. Associated high-pressure units yield Early–Late Cretaceous ages [21]. Final ocean closure occurred during the Latest Cretaceous–Early Paleocene, followed by Cenozoic dextral strike-slip faulting [22].

Late Eocene intrusions in the Lut Block are calc-alkaline (non-adakite; low Sr/Y ratios) and host diverse porphyry–epithermal Au–Cu systems [23] and references therein. In contrast, high-grade Cu-rich porphyries in the Urumieh-Dokhtar magmatic arc (UDMA; Group I) are linked to adakite-like suites (e.g., high Sr/Y ratios), whereas older Eocene–Oligocene deposits (Group II) are sub-economic and related to non-adakitic magmas emplaced before final Neotethyan closure. Despite coeval arc magmatism, significant Au mineralization—including porphyry Au–Cu (e.g., Shadan and Maherabad), breccia-pipe (e.g., Khunik), reduced intrusion-related gold (Hired), and iron oxide–copper–gold (IOCG)–epithermal hybrid systems (e.g., Qaleh Zari and Godakan)—occurs exclusively in the Lut Block. These formed under extensional to transtensional conditions induced by slab rollback or steepening, which promoted asthenospheric upwelling, crustal thinning, and lower-crustal magma accumulation. Deep transcrustal faults such as Nayband and Nehbandan provided efficient conduits for magma ascent and Au-bearing fluid flow, enhancing ore formation in the Lut Block.

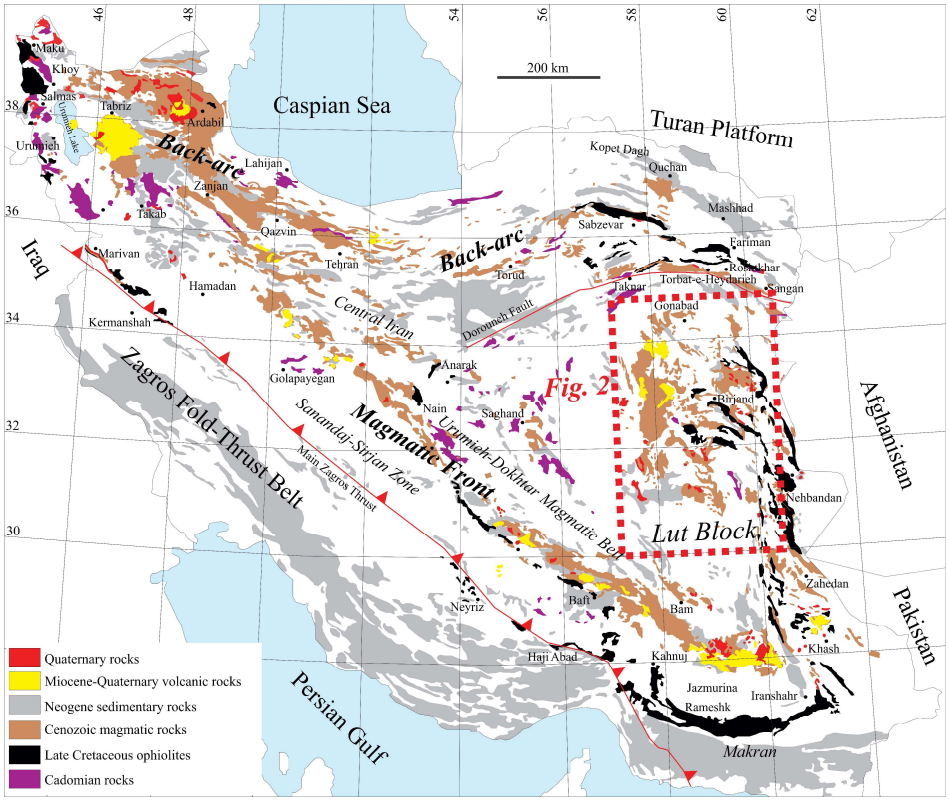


Figure 1. A simplified structural map of Iran highlighting the main tectonic units, modified from [21].

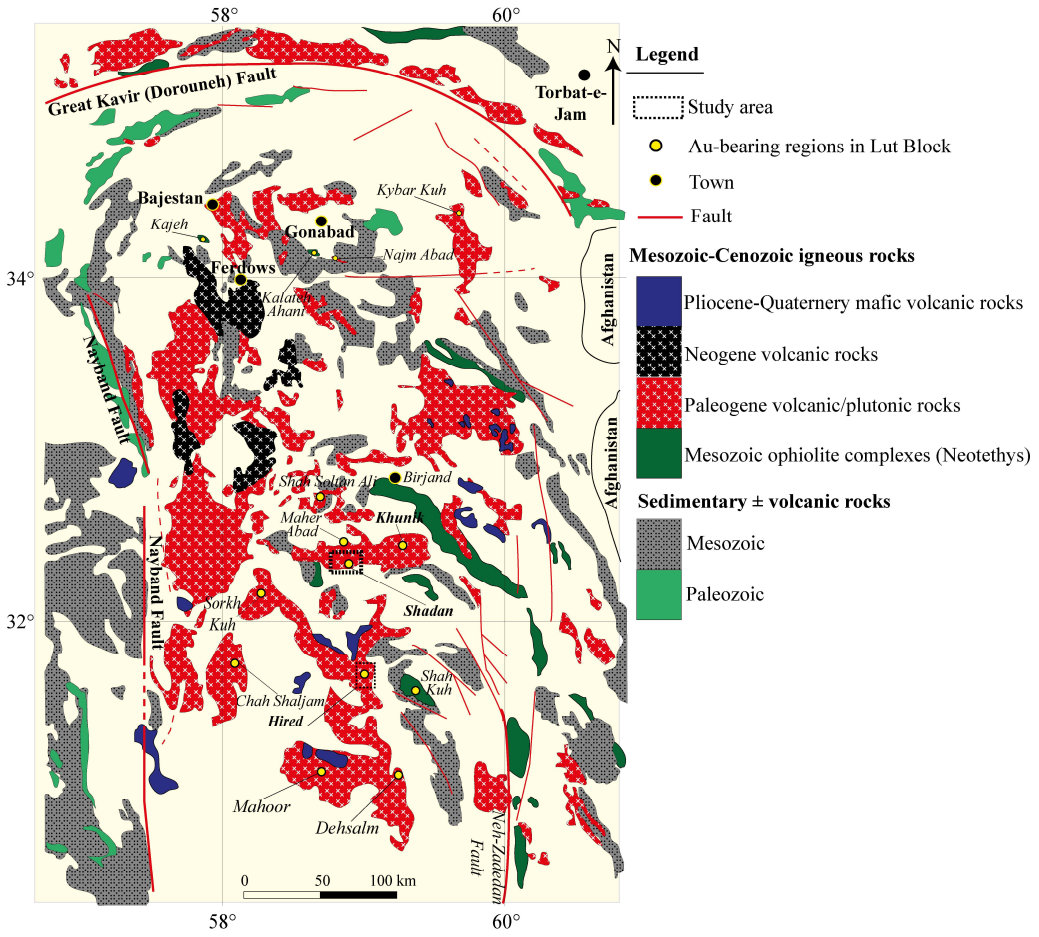


Figure 2. Geological map of the Lut Block, modified from [21].

2. Regional Geology, Metallogeny and Relevance to Shadan

The Shadan area lies roughly 60 km southwest of Birjand, within the central Lut Block, where a belt of volcanic–plutonic complexes is exposed in an NW–SE trend (Figure 2). The oldest exposed units in this region comprise Eocene lavas (e.g., basaltic andesite to andesite flows and lithic tuffs), which are locally overlain by younger volcanic rocks. Detailed field observations in Shadan document the presence of diorite to granodiorite plutonic intrusions (Appendix A Figure A1) and crosscut by quartz–carbonate vein networks. Zircon U–Pb ages indicate emplacement at ~39–37 Ma [23]. Several E–W striking mafic to intermediate dikes (basaltic to basaltic andesite) cut these plutonic rocks, suggesting a younger magmatic pulse emplaced after the main plutonic bodies.

The Shadan deposit contains an estimated 57 Mt of ore at 0.55 g/t Au, classifying it as an Au–Cu porphyry system, albeit with a relatively low Cu/Au ratio (~0.27). Copper mineralization is dominated by chalcopyrite and malachite, while magnetite represents a significant Fe phase, occurring as massive veinlets and disseminations. As illustrated in Figure 3, pyrite is the most abundant sulfide, occurring in disseminations, veinlets, quartz–pyrite veins, and occasionally within hydrothermal breccias. Shadan exemplifies a structurally controlled, multi-stage porphyry system, exhibiting classic hydrothermal zonation. Ore mineralization at Shadan comprises both hypogene and supergene components. Hypogene sulfides include pyrite, chalcopyrite, covellite, and magnetite, whereas supergene assemblages consist of malachite, azurite, chrysocolla, hematite, and other Fe oxides–hydroxides. Copper occurs primarily as chalcopyrite in hypogene zones and as malachite or chrysocolla in fractures and minor veinlets. Gold is concentrated within Fe oxides–hydroxides derived from pyrite oxidation [23]. Mineralization is structurally controlled along steeply dipping NW–SE–trending structures and occurs as vein–veinlet stockworks, hydrothermal breccias, and disseminations, with stockworks representing the dominant ore volume. Sheeted quartz ± anhydrite veins associated with multi-stage intrusions act as principal conduits for ore fluids. High-density, high-volume vein zones in the deposit display a NW–SE orientation, closely linked to transpressional faulting. Such a compressional regime initially limited the upward migration of ore-forming fluids, with subsequent local stress changes promoting fluid depressurization and channeling along these faults, forming sheeted vein networks [23]. This highlights the critical role of transpressional structures in localizing and controlling mineralization, with significant implications for regional porphyry exploration. Integration of vein spatial distribution with lithogeochemical gold anomalies using fractal modeling reveals that areas combining high vein density and volume with gold enrichments represent zones of enhanced exploration potential at both deposit and regional scales.

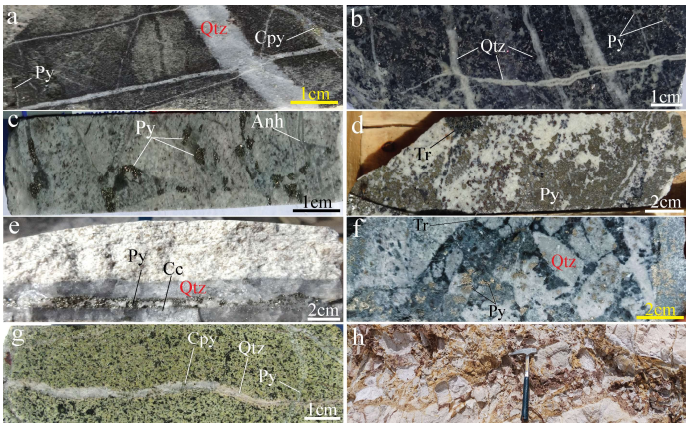


Figure 3. Field and hand-specimen examples illustrating the range of quartz–sulfide vein types and mineralization characteristics in the Shadan Au–Cu epithermal system with porphyry affinity.

(**a**,**b**) Qtz veins intersecting altered country rocks that host disseminated Py and Cpy. (**c**,**d**) Py-bearing veinlets and disseminated mineralization within altered rocks, locally associated with Anh and Tr. (**e**,**f**) Qtz ± Cc veins displaying Py ± Cpy mineralization and heterogeneous wall-rock alteration signatures. (**g**) Altered volcanic host containing a Py- and Cpy-bearing quartz vein. (**h**) Stockwork arrays of quartz–carbonate vein and veinlet networks within the Shadan deposit. Each panel contains a scale bar. Abbreviations: Py: pyrite; Cpy: chalcopyrite, Anh: anhydrite; Tr; tourmaline; Qtz: quartz; Cc: carbonate.

3. Methodology

This study integrates field-based spectral measurements with laboratory petrological and geochemical analyses to characterize alteration mineralogy and classify spectral–lithological groups in the Shadan epithermal system. The workflow involved systematic sampling, spectral acquisition, petrographic observations, XRD validation, and geochemical assays to ensure robust mineral identification and group assignment.

3.1. Field Sampling and Spectral Measurements

A total of 38 representative rock samples were collected from the principal alteration zones of the Shadan epithermal system and analyzed through an integrated spectroscopic, petrographic, mineralogical, and geochemical workflow. Lithological and alteration zones were delineated through the integration of field-based lithological mapping, petrographic observations, VNIR–SWIR spectral characteristics, and remote sensing interpretations, supported by available technical datasets provided by Karand Sadr Jahan Mines and Mineral Industries Co., Laboratory analyses included X-ray fluorescence (XRF) using an Olympus Vanta handheld unit (Olympus Corporation, Boston, MA, USA), ICP-MS using an Agilent 7900 system (Agilent Technologies, Santa Clara, CA, USA), petrographic examination with an Olympus BX51 microscope (Olympus Corporation, Tokyo, Japan), and XRD phase identification using a Bruker D8 Advance diffractometer (Bruker AXS GmbH, Karlsruhe, Germany). VNIR–SWIR reflectance spectra (0.35–2.50 μm) were acquired with a calibrated ASD FieldSpec 4 Hi-Res spectrometer (Malvern Panalytical, Malvern, UK) equipped with a halogen light source and contact probe. A Spectralon® white reference panel was measured before each batch for calibration, and three to five scans were collected per specimen and averaged to minimize noise and instrumental variability.

The study employed 38 strategically selected samples, reflecting a targeted, rather than statistical, sampling strategy, optimized for characterizing and classifying hydrothermal alteration types rather than quantifying mineral abundances or geochemical gradients across the deposit. The sample selection prioritized representativeness over numerical abundance, ensuring that each alteration type—argillic, advanced argillic, silicified, Fe-oxide, oxidized argillic, propylitic, and carbonate–iron assemblages—was represented by 4–6 samples, capturing intra-type variability. This approach aligns with established protocols in hydrothermal alteration studies, where 30–50 well-chosen samples typically suffice to delineate alteration mineralogy and zonation in porphyry–epithermal systems e.g., [11]. Each sample was analyzed using four complementary techniques (VNIR–SWIR spectroscopy, petrography, XRD, and whole-rock geochemistry), providing multi-dimensional validation. Consistency between spectral groupings and independently derived mineralogical and geochemical data confirms that the dataset adequately captures the principal alteration assemblages. Samples were spatially distributed along key structural trends, lithological contacts, and alteration boundaries identified in prior field mapping (Figure 4). This transect-style design captures both hypogene and supergene domains without requiring dense sampling of homogeneous zones. And, the 38-sample dataset is consistent with previous integrated hydrothermal studies, where combined spectral–mineralogical–

geochemical approaches typically use 25–50 specimens e.g., [16], reflecting the diminishing informational returns of additional sampling once the main alteration facies and their spectral–mineralogical signatures are established. Therefore, the combination of strategic sample selection, multi-method validation, and comprehensive coverage of all alteration types provides a robust framework for spectral–lithological classification, supporting the interpretation of hydrothermal processes in the studied system.

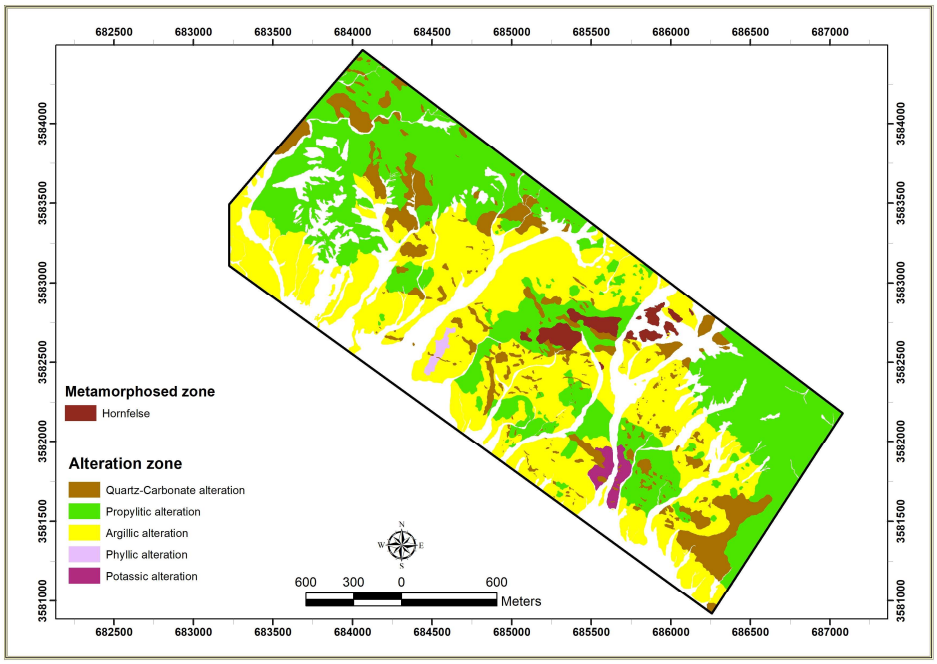


Figure 4. Spatial distribution of alteration and lithological units within the study area, including quartz–carbonate, argillic, propylitic, phyllic, potassic, and localized hornfels zones. The arrangement highlights structural influences, fluid-flow pathways, and supergene effects aligned with lithological–spectral groups G_1–G_7.

Raw VNIR–SWIR spectra were first inspected for instrument noise and illumination artifacts, then corrected using white-reference normalization and resampled to uniform spectral intervals. A Savitzky–Golay smoothing filter was applied to suppress high-frequency noise without distorting absorption geometry [3,10]. Continuum removal was performed using convex-hull normalization to enhance mineral-specific diagnostic features [9,24]. Feature extraction focused on the principal absorption regions known to characterize hydrothermal alteration minerals in epithermal–porphyry systems: (i) ~1.40 and ~1.90 µm: vibrational overtones of structural and adsorbed OH/H_2O in clays and altered volcanics; (ii) ~2.20 µm: Al–OH absorptions indicative of illite, kaolinite, and sericite; (iii) 2.25–2.35 µm: Mg–Fe–OH bands associated with chlorite and epidote; (iv) 2.30–2.35 µm and ~2.50 µm: CO_3 absorptions characteristic of calcite and dolomite; and (v) ~0.90 µm: Fe^{3+} crystal field transitions in hematite and goethite. For each spectrum, band depth, absorption minimum (λc), full-width geometry, and shoulder position were calculated and compiled as inputs for downstream classification. This workflow follows established protocols in spectral geology and alteration mapping [4,11,16,17]. For spectral visualization, groups G_1–G_3 (n = 6 each) are shown with all individual spectra to capture intra-group variability in absorption features, while groups G_4–G_7 (n = 1–3) are represented by median spectra due to high spectral homogeneity and limited sample numbers. This dual strategy balances completeness and clarity, highlighting diagnostic absorption features without redundancy. All spectral assignments were validated against XRD mineralogy and whole-rock geochemistry, ensuring robust and reproducible alteration group definitions.

Spectral classification followed a hybrid workflow integrating unsupervised clustering with expert-guided feature interpretation. Hierarchical agglomerative clustering was initially applied to the preprocessed spectra using key diagnostic parameters, including absorption minima (e.g., $\lambda c_{2.20}$ and $\lambda c_{2.30}$), band depth ($BD_{2.20}$ and $BD_{2.30}$), hydration indices, and Fe-related spectral metrics. These features served to distinguish clay-rich, carbonate-bearing, quartz-dominant, Fe-oxide, and propylitic assemblages consistent with epithermal hydrothermal zonation [8,9,11]. For visualization and validation, two spectral products were generated per group: (i) a stacked spectral mosaic to examine internal variability and outlier behavior, and (ii) an averaged representative spectrum highlighting diagnostic absorption geometry and continuum shape. This approach ensured both spectral consistency and geological plausibility in group assignment [4,6,14].

Radar diagrams were generated from processed VNIR–SWIR spectral datasets to facilitate comparative visualization of diagnostic absorption features across alteration groups. Spectral band depths were normalized to a 0–1 scale prior to plotting. Data visualization and analytical plotting were performed using standard Python 3.11-based tools (Matplotlib 2025b) under an institutional academic license (Sheffield Hallam University).

3.2. X-Ray Diffraction (XRD) Mineralogical Validation

Powder XRD analyses were performed on representative samples from each spectral group at the University of Tehran using a Bruker D8 Advance diffractometer (Bruker AXS, Karlsruhe, Germany) equipped with CuKα radiation ($\lambda K\alpha_1$ = 1.5406 Å) and a Ni filter to suppress CuKβ radiation. The instrument was operated at 40 kV and 40 mA. Diffraction data were collected over a 2θ range of 5–70° with a step size of 0.02° and a counting time of 1 s per step. The incident beam optics included a fixed divergence slit of 0.6° and a 0.1 mm receiving slit. Bulk samples were crushed and pulverized in an agate mill to <75 µm to minimize preferred orientation. Powder mounts were prepared using the back-loading technique to ensure random grain orientation. Mineral phases were identified by comparison with the PDF-4 database of the International Centre for Diffraction Data (ICDD). Diffractograms were processed to identify primary and secondary mineral phases associated with alteration, including illite, kaolinite, chlorite, quartz, calcite, dolomite, and hematite. Particular attention was given to mineral pairs with overlapping VNIR–SWIR spectral features (e.g., illite vs. kaolinite; calcite vs. dolomite), allowing XRD results to resolve spectral ambiguities and confirm diagnostic absorptions. These mineralogical constraints were used to validate group assignments and strengthen the interpretation of hydrothermal processes when integrated with petrography and spectral feature analysis [11].

3.3. Whole Rock Geochemistry

Major element concentrations in whole-rock powders were determined using a Rigaku Primus II XRF spectrometer at Wuhan Sample Solution Analytical Technology Co., Ltd., Wuhan, China. The analytical protocol was as follows: (1) powdered samples (200 mesh) were oven-dried at 105 °C for 12 h; (2) approximately 1.0 g of the dried material was weighed into a ceramic crucible and heated in a muffle furnace at 1000 °C for 2 h. After cooling to ~400 °C, the crucibles were transferred to a desiccator, reweighed, and the loss on ignition (LOI) was calculated; (3) 0.6 g of sample powder was thoroughly mixed with 6.0 g of flux ($Li_2B_4O_7$:$LiBO_2$:LiF = 9:2:1) and 0.3 g of oxidizer (NH_4NO_3) in a platinum crucible, then fused at 1150 °C for 14 min. The melt was rapidly cooled in air to form flat glass discs, which were subsequently analyzed by XRF. Trace element compositions were determined using an Agilent 7900 inductively coupled plasma–mass spectrometer (ICP–MS) at the same laboratory. The digestion and analytical procedure was as follows:

(1) powdered samples (200 mesh) were oven-dried at 105 °C for 12 h; (2) 50 mg of dried powder was placed in a Teflon bomb, to which 1 mL of HNO_3 and 1 mL of HF were added; (3) the sealed bombs were enclosed in stainless-steel jackets and heated in an oven at 190 °C for more than 24 h; (4) after cooling, the solutions were evaporated to near dryness on a hotplate at 140 °C, followed by the addition and evaporation of 1 mL HNO_3; (5) 1 mL of HNO_3, 1 mL of Milli-Q water, and 1 mL of internal standard solution containing 1 ppm indium were then added. The bombs were resealed and reheated at 190 °C for over 12 h; (6) the resulting clear solutions were transferred to polyethylene bottles and diluted to 100 g using 2% HNO_3. The analytical uncertainties are generally within ±1% for major oxides and better than ±5% for trace elements.

Spectral, petrographic, XRD, and geochemical datasets were cross-validated to ensure internal consistency in the classification of alteration groups. Absorption features identified in VNIR–SWIR spectra were matched with mineral phases confirmed by XRD, particularly in cases where clays, carbonates, or Fe-oxides exhibited overlapping diagnostic bands. Geochemical parameters were evaluated alongside spectral metrics, including correlations between Al_2O_3 and K_2O with $BD_{2.20}$ and $\lambda c_{2.20}$, and between Fe_2O_3 and the Fe-index near ~0.90 μm. Petrographic observations were used to reconcile spectral signatures with mineral replacement textures, alteration microfabrics, and paragenetic relationships. For each group, averaged representative spectra were annotated with absorption features linked directly to mineralogical and geochemical controls, providing a robust basis for classification and interpretation.

4. Results and Discussion

The seven lithological–alteration groups (G_1–G_7) were defined a priori based on mineral assemblages, fluid–rock reaction pathways, and their spectral signatures, rather than by unsupervised clustering of field data. These groups reflect the evolutionary sequence and physicochemical gradients of low-sulfidation epithermal systems developed in volcanic and plutonic settings. Each group is evaluated in terms of its mineral assemblages confirmed by XRD and petrography, major- and trace-element geochemistry, and diagnostic VNIR–SWIR absorption features. The following subsections present geochemical trends, mineralogical signatures, and spectral characteristics for each group, highlighting their genetic relationships and spatial associations within the hydrothermal system. It should be noted that the seven alteration groups defined here are based on 38 strategically selected samples, designed to capture the principal alteration types across the Shadan system, as justified in Section 3.1. Although the sample density is insufficient for detailed statistical modeling of geochemical gradients, the consistency between spectral classifications and independently derived mineralogical and geochemical datasets demonstrates that the collection adequately represents the major alteration facies and their diagnostic signatures.

Representative field and hand-specimen photographs illustrate the characteristic lithologies and alteration textures of the seven alteration groups (G_1–G_7). The spatial distribution of hydrothermal alteration and lithological zones within the Shadan system defines a coherent zonation pattern controlled by structure, lithology, and fluid pathways. Quartz–carbonate, argillic, propylitic, phyllic, and potassic alteration domains, together with localized hornfels metamorphic zones, form a systematic arrangement that reflects both hypogene alteration processes and subsequent supergene overprinting. This alteration architecture provides the spatial framework for the classification of the seven lithological–spectral groups (G_1–G_7) described below (Figure 4).

4.1. Mineralogy

Mineralogical characterization of the Shadan hydrothermal system was conducted through integrated petrographic observations and XRD analyses of representative samples from all seven alteration–lithological groups (G_1–G_7) (see Figures 5–7). Petrographic examination of thin sections provides direct textural and mineralogical evidence for the alteration processes inferred from spectral and geochemical data. Representative photomicrographs from all seven alteration–lithological groups (G_1–G_7) illustrate systematic variations in primary mineral replacement, alteration intensity, and mineral assemblage evolution across the hydrothermal system. These observations document the progression from clay-rich argillic and silicified domains to carbonate–Fe-oxide–bearing assemblages and distal propylitic overprints, and form the petrographic basis for linking alteration facies with diagnostic VNIR–SWIR spectral features and bulk-rock geochemical trends. The combined dataset allows clear differentiation between clay-rich argillic halos, silicified cores, carbonate-bearing transitions, Fe-oxide caps, and propylitic envelopes. Each group exhibits a distinct mineral assemblage that reflects variations in fluid chemistry, temperature, and water–rock interaction. To document these domains, a representative XRD pattern was selected for each group and is presented ahead (Figure 7).

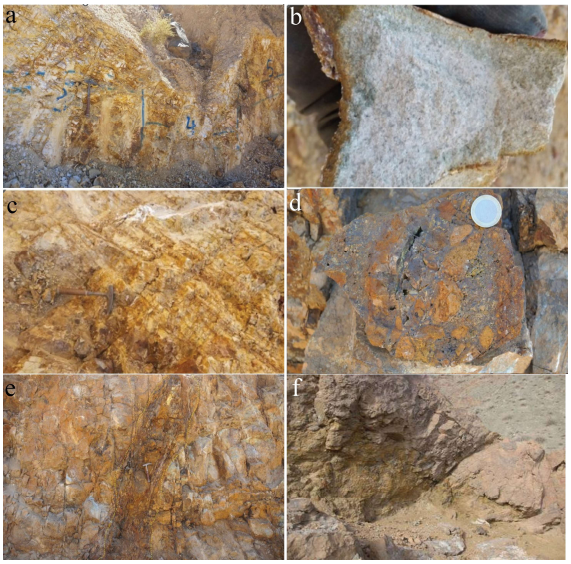


Figure 5. Field photographs illustrating key alteration features and their corresponding groups. (**a**) Argillic alteration with abundant clay mineral development (G_1). (**b**) Interface zones between the G_1 argillic center and surrounding carbonate-bearing units. (**c**) Carbonate and iron oxide veinlets overprinting argillic assemblages. (**d**) Highly oxidized supergene assemblages formed through oxidative weathering of sulfides and Fe-bearing silicate/carbonate phases. (**e**) Argillic alteration in an oxidized state, marked by clay-rich assemblages partially overprinted by supergene hematite and goethite. (**f**) Quartz–carbonate veins partially overprinted by iron oxides.

G_1 represents the dominant argillic halo developed within vitric tuffs and altered volcaniclastic units. This zone is marked by pervasive feldspar replacement, fluid-assisted leaching, and phyllosilicate assemblage (e.g., mixed-layer of kaolinite–sericite–illite–smectite), consistent with near-surface acidic alteration in low-sulfidation environments (Figures 5a and 7a) [16,25]. The mineralogical suite is characteristic of the intermediate argillic to advanced argillic transition commonly identified in such environments through SWIR spectroscopy [26]. Field mapping shows G_1 along fracture-controlled zones and shallow stratabound domains, commonly adjacent to phyllic and carbonate-bearing assemblages. Textures record pervasive feldspar replacement and pervasive leaching, with illitization of feldspars and partial preservation of vitric volcanic textures (Figure 6). Quartz

is present as fine-grained mosaics or relict grains. Mafic phases show either chloritization or pervasive alteration to fine phyllosilicates and oxides rather than sericitization. Minor hematite and pyrite relicts occur locally. The argillic mineral assemblage inferred from field observations and petrographic textures is further supported by X-ray diffraction results. Representative XRD patterns for G_1 confirm the dominance of illite–smectite mixed layers with kaolinite, consistent with pervasive feldspar alteration and clay mineral development observed in the field (Figure 5a). X-ray diffraction analysis of representative G_1 samples confirms the dominance of clay-rich argillic mineral assemblages inferred from field observations and spectral characteristics. The XRD pattern of Sample 01 (Az:1382-1) reveals kaolinite and quartz as the principal phases, with minor illite, validating the interpretation of an argillic alteration halo developed under acidic, near-surface conditions (Figure 7a). The mineralogy is consistent with shallow argillic alteration; the relative abundance of kaolinite in some samples suggests localized intense leaching or acid overprinting rather than wholesale high-sulfidation conditions [8,11].

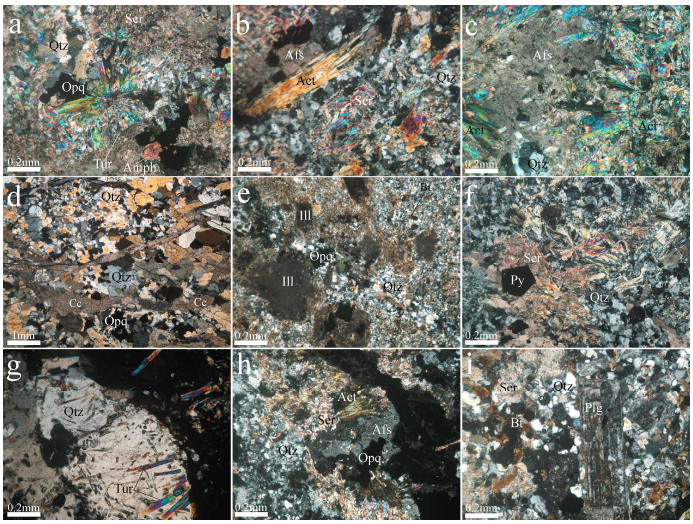


Figure 6. Representative field and hand-specimen photographs illustrating quartz–sulfide vein systems and mineralization styles in the Shadan Au–Cu epithermal system with porphyry affinity. (**a**,**b**) Quartz veins crosscutting altered host rocks with disseminated pyrite and chalcopyrite. (**c**,**d**) Pyrite-bearing veins and disseminations within altered rocks, locally associated with anhydrite and tourmaline. (**e**,**f**) Qtz ± Cc veins exhibiting Py ± Cpy mineralization and variable wall-rock alteration. (**g**) Quartz vein hosting chalcopyrite and pyrite within altered volcanic lithologies. (**h**) Field-scale quartz–carbonate vein networks forming vein–veinlet stockworks within the Shadan deposit. (**i**) Photomicrograph showing sericitic alteration characterized by fine-grained sericite (Ser) replacing plagioclase (Plg), associated with quartz (Qtz) and minor biotite (Bt), indicative of hydrothermal overprint.

G_2 occupies transition zones between the argillic core (G_1) and carbonate-rich structural corridors (Figure 5b) and is common along fracture selvages, shallow breccias and permeable tuffs. Petrography and XRD show coexistence of phyllosilicates (dominantly illite-smectite mixed-layers), fine calcite, and dolomite (Figure 7b). This mineral association is consistent with neutralization and cooling of hydrothermal fluids and is commonly interpreted as a peripheral or shoulder assemblage in porphyry–epithermal systems [25]. The interpretation of CO_2-buffering (fluid pH increase) is supported here by elevated CaO–MgO and Sr contents in G_2 samples; direct fluid inclusion or C-isotope evidence would be required to confirm fluid CO_2 abundance [27]. Microtextures include moderate feldspar replacement by illite and carbonate cementation that locally obscures primary fabric. Disseminated opaque minerals are rare; pyrite ghosts record earlier sulfide deposition.

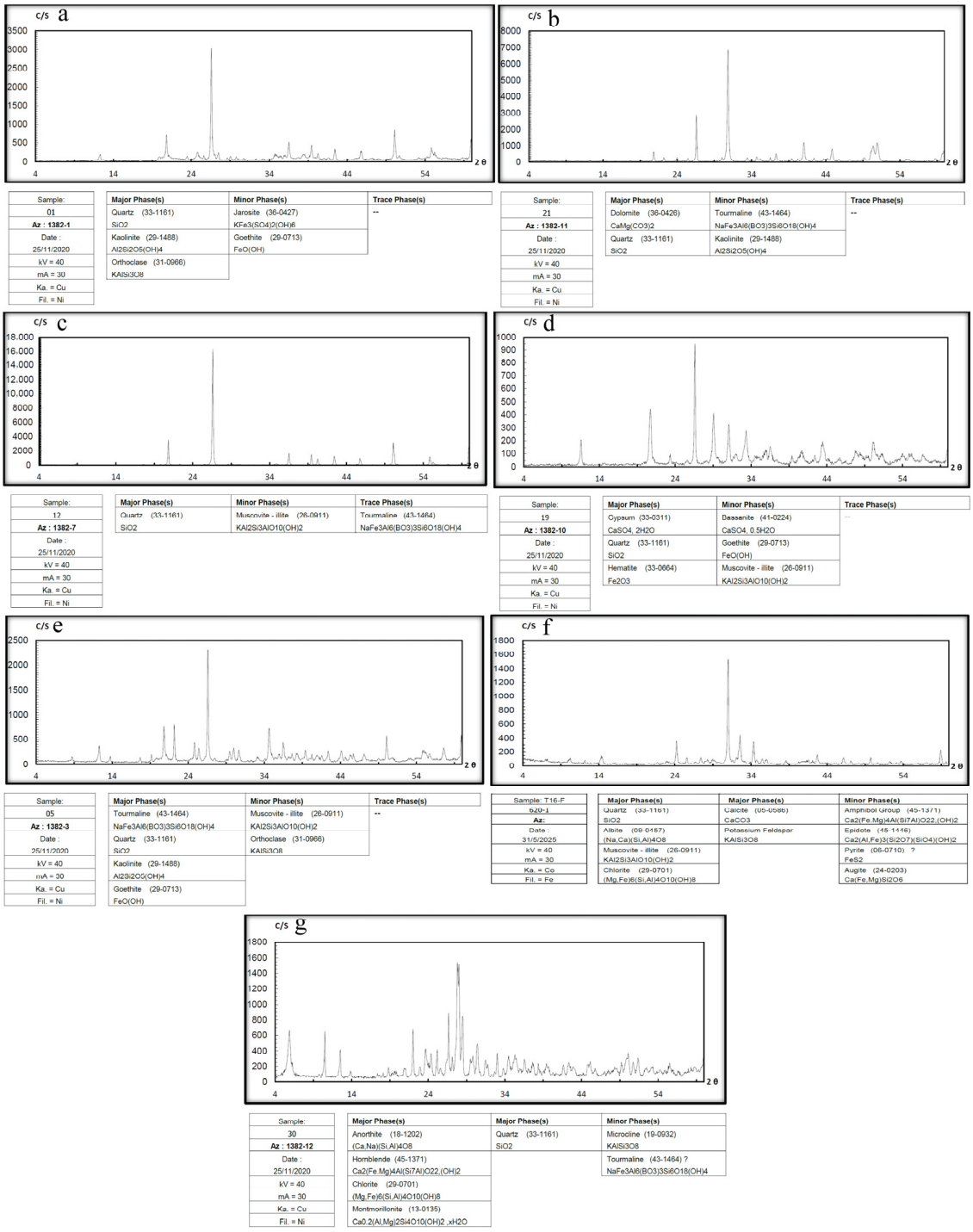


Figure 7. X-ray diffraction analyses conducted on representative samples across the seven alteration–lithological groups (G_1–G_7). (**a**) XRD pattern of sample 01 showing major phases of quartz, kaolinite, and orthoclase, with minor jarosite, K-feldspar, and goethite (G_1). (**b**) XRD pattern of sample 11 characterized by calcite and quartz as major phases, with minor Na-feldspar and kaolinite (G_2). (**c**) XRD pattern of sample 7 dominated by quartz, with minor muscovite–illite and trace tourmaline (G_3). (**d**) XRD pattern of sample 19 showing gypsum, quartz, and hematite as major phases, with minor bassanite, goethite, and muscovite–illite (G_4). (**e**) XRD pattern of sample 05 characterized by tourmaline and quartz as major phases, with minor muscovite–illite, orthoclase, kaolinite, and goethite (G_5). (**f**) XRD pattern of sample 620-1 dominated by quartz and calcite, with subordinate albite, muscovite–illite, chlorite, amphibole group minerals, pyrite, and augite (G_6). (**g**) XRD pattern of sample 30 characterized by anorthite, hornblende, and chlorite as major phases, with quartz and microcline as subordinate components and minor tourmaline (G_7).

G_3 corresponds to strongly silicified domains linked to hydrothermal upflow zones, stockworks, and silicic caps. Such zones form where silica-rich fluids replace primary mineralogy or infill open spaces [25,28]. Field observations show that silicified domains commonly develop as linear quartz–carbonate zones aligned with major structural trends, reflecting focused hydrothermal upflow and permeability-controlled fluid pathways (Figure 5c). X-ray diffraction analysis of representative G_3 samples confirms the mineralogical simplicity of these domains, with the XRD pattern of Sample 12 (Az:1382-7) dominated by quartz and only minor muscovite–illite, consistent with pervasive silicification and minimal clay development (Figure 7c). These vuggy and massive silica zones are often interpreted as the roots of lithocaps, formed by acidic magmatic-hydrothermal fluids in the upper parts of porphyry–epithermal systems [25]. Petrographic observations include pervasive silicification with complete or partial obliteration of host textures. Quartz occurs as microcrystalline aggregates, chalcedony, or granular veinlets. Feldspars and ferromagnesian minerals are extensively replaced. Clay minerals are scarce and typically restricted to microfractures. Minor hematite may occur as late oxidation products. Spectrally, G_3 exhibits feature-poor reflectance with absent or very weak hydroxyl groups (–OH) and CO_3 absorptions, characteristic of quartz-rich lithologies [3,11]. G_3 is clearly distinguished from $G_1/G_2/G_5$ (clay-bearing) and G_6 (chlorite–epidote).

G_4 comprises strongly oxidized supergene zones formed through weathering of sulfides and Fe-bearing silicates or carbonates (Figure 5d). These zones are typical of near-surface conditions over shallow epithermal or porphyry systems [29–31]. Field overview along with petrography and XRD data (Figure 7d) show hematite and goethite as dominant phases (hematite as earthy masses and coatings; goethite as botryoidal/fibrous aggregates). These caps overprint earlier hydrothermal assemblages via meteoric oxidation and leaching, and their development is supported by elevated Fe_2O_3, depletion in mobile base metals in the oxide cap itself, and enrichment of redox-sensitive elements (As and Mn) in adjacent soils and rinds. Relative to argillic (G_1–G_2) and intermediate/propylitic (G_3) halos, G4 marks the uppermost oxidative environment where meteoric water–rock interaction and redox gradients dominate, overprinting prior hydrothermal assemblages.

G_5 represents oxidized argillic alteration where clay-rich assemblages (e.g., illite–smectite ± kaolinite) have undergone partial supergene overprinting, incorporating hematite and goethite (Figure 5e). These zones commonly form near paleosurfaces or along oxidation pathways. This mineralogical association is characteristic of the "oxide-argillic" transition, where the VNIR-SWIR spectral response is a composite of Fe-oxides/oxyhydroxides and phyllosilicate features, a key indicator in weathered terrains [32]. Petrography and XRD data records replacement of volcanic glass and feldspar by clays with pervasive Fe-oxide impregnation (Figure 7e). Hematite occurs as grain coatings, earthy masses, or fracture infillings; goethite appears as fibrous or patchy replacements. Quartz occurs in minor amounts as relicts or veinlets.

G_6 corresponds to the outer propylitic halo along the margins of volcanic and intrusive rocks, formed by neutral to slightly alkaline fluids at lower temperatures (commonly <~250–300 °C) [29]. The characteristic mineral assemblage of chlorite, epidote, and albite is diagnostic of the distal, low-temperature expression of magmatic-hydrothermal systems, as defined in comprehensive alteration models [33]. Thin-section observations reveal partially preserved igneous textures. Feldspars exhibit patchy epidote and calcite replacement, while ferromagnesian minerals are replaced by chlorite ± tremolite–actinolite. Quartz is interstitial and weakly recrystallized. Sulfides are rare, and Fe-oxide content is low.

G_7 comprises quartz–carbonate veins with variable iron-oxide overprinting (Figures 5f and 7g). These late-stage hydrothermal veins cut earlier alteration halos and acted as late-stage structural conduits for fluid flow [25]. Such carbonate-base metal gold

(CBMG) or intermediate-sulfidation style veins are typical of the periphery of porphyry–epithermal systems, where cooler, neutral-pH fluids deposit carbonate and quartz [34]. Petrography and geochemistry show calcite ± dolomite dominance with subordinate quartz; hematite frequently rims or stains vein margins where post-depositional oxidation affected sulfide-rich veins. The veins are interpreted as late hypogene to near-surface veinage, commonly associated with cooler, near-neutral fluids.

4.2. Geochemistry

G_1 samples (argillic; mixed-layer illite–smectite and kaolinite) were collected from clay-rich argillic halos developed within altered tuff and andesitic units. The major-oxide compositions are characterized by elevated Al_2O_3–K_2O ratios, depleted Na_2O, moderate Fe_2O_3 contents, and increased LOI values (Table 1). This geochemical signature is diagnostic of hydrolytic alteration, where plagioclase destruction releases Ca and Na, while K, Al, and H_2O are fixed in illitic clays. Trace element patterns commonly show elevated As and moderate Au–Cu concentrations, consistent with argillic alteration zones formed adjacent to quartz–sulfide vein systems. Elevated Al_2O_3–K_2O coupled with depleted Na_2O contents confirms sericitic alteration along with illite. The increased LOI values correspond to structurally bound hydroxyl and molecular water. Elevated As associated with moderate Au–Cu values indicates proximity to quartz–carbonate vein structures, but without significant carbonate addition—clearly distinguishing these samples from the G_2 and G_7 groups. The enrichment of As, a common pathfinder element, alongside Au–Cu in these advanced argillic environments is a well-documented exploration vector [35].

G_2 (i.e., argillic + carbonate; illite/kaolinite ± calcite/dolomite) geochemistry shows elevated CaO and MgO, moderate K_2O–Al_2O_3 contents, and enrichment in Sr, reflecting carbonate overprinting (Table 1). The combined increases in CaO–MgO, Sr, and LOI values support carbonate overprinting on an argillic substrate and are consistent with fluid neutralization or mixing at structural conduits [36]. Trace metal contents (Au–As–Cu) remain moderate, consistent with mineralization along neutralization fronts and fluid–rock mixing or buffering zones adjacent to vein systems. G_2 differs from G_7 in being wall-rock-controlled rather than vein-dominated.

G_3 (i.e., silicic/quartz-rich) major-oxide compositions exhibit very high SiO_2 contents, low Fe, Mg, and Ca, and modest K_2O (~1%), reflecting adularia–sericite selvages along vein margins. The pronounced SiO_2 enrichment confirms extensive silica flooding and stockwork development (Table 1). This intense silicification is a hallmark of the highest permeability zones in hydrothermal systems, where large fluid fluxes lead to quartz precipitation and the formation of resistant lithological and geochemical anomalies [37]. Trace metal concentrations (Au–As–Cu) are generally moderate, while Au shows variability depending on vein density. These features suggest that structural corridor density and associated Au–As–Cu trends are critical parameters for delineating mineralized zones.

G_4 (i.e., iron-oxide rich; hematite and goethite) geochemistry shows elevated Fe_2O_3, moderate SiO_2, and minor Ca–Mg contents, reflecting pervasive oxidation and Fe-oxide enrichment. The development of iron oxide-rich assemblage is a key supergene process, forming a distinct lithogeochemical halo that serves as a first-order guide to underlying mineralization [38]. Trace element data display redox-sensitive behavior, with moderate Au and Cu concentrations where relict sulfides persist, and enrichment in As and Mn commonly associated with oxide blankets (Table 1). The pronounced Fe_2O_3 increase confirms hematite–goethite dominance, while moderate As–Au–Cu values indicate supergene overprinting of hypogene vein systems. G_4 assemblages therefore provide an effective geochemical vector toward deeper sulfide-bearing zones.

Table 1. Representative whole rock major and trace element compositions of Shadan region.

Sample	Group	SiO_2	Al_2O_3	Fe_2O_3	CaO	MgO	K_2O	Na_2O	TiO_2	MnO	LOI	Total	Au	Ag	As	Cu	Mo	Pb	Zn	Sb	Sr	Ba	Rb	Cs
							wt.%						ppb	ppm	ppm	ppm	ppm	ppm	ppm	ppm	ppm	ppm	ppm	ppm
SHD-G1-01		65.4	17.3	5.02	1.69	1.13	3.31	1.26	0.54	0.05	4.84	100.5	212	1.73	820	266	8.13	24.5	72.13	2.91	181	413	96.3	8.32
SHD-G1-02		63.1	18.4	4.83	2.18	1.27	3.74	0.82	0.61	0.06	5.16	100.2	189	2.08	903	284	7.64	25.7	79.35	3.20	165	439	126	7.94
SHD-G1-03		66.8	16.2	4.36	1.49	0.98	3.27	1.53	0.52	0.03	5.09	100.3	326	2.61	1184	349	8.59	28.7	88.26	3.38	159	358	132	9.45
SHD-G1-04		62.9	18.9	4.61	2.38	1.16	3.66	0.94	0.64	0.04	4.95	100.1	164	1.77	765	198	6.44	21.2	70.21	2.23	205	425	118	7.78
SHD-G1-05		64.3	17.1	3.72	1.94	0.87	3.54	1.22	0.42	0.02	7.1	100.2	241	1.95	988	315	8.91	20.7	76.34	3.27	177	402	127	8.94
SHD-G1-06		63.3	18.8	4.18	1.54	1.32	2.91	0.87	0.73	0.05	6.37	100	288	3.40	1052	484	5.96	19.6	81.84	2.75	213	371	149	10.2
SHD-G2-01		58.7	15.9	3.99	6.44	2.36	2.96	0.91	0.48	0.05	8.71	100.4	269	1.54	653	313	7.29	13.3	68.54	2.66	421	336	92.4	7.56
SHD-G2-02		56	16.6	4.13	7.23	3.11	2.62	0.88	0.52	0.04	8.94	100.1	194	1.55	584	267	6.94	20.2	71.45	2.38	197	327	78.6	6.68
SHD-G2-03	G2	60.3	15.4	3.28	5.94	1.97	1.87	1.23	0.56	0.03	9.67	100.2	271	1.72	725	319	5.79	23.6	80.95	2.51	395	369	95.3	8.13
SHD-G2-04		57.4	16.9	4.57	6.72	2.54	2.91	0.72	0.57	0.06	8.31	100.6	209	1.33	619	238	6.35	19.1	67.09	2.43	446	298	90.1	7.64
SHD-G2-05		59.3	15.7	3.65	6.11	2.21	2.67	0.95	0.58	0.04	8.9	100	235	1.68	698	288	7.48	17.1	75.13	3.14	415	355	101	6.29
SHD-G3-01		88	5.36	1.29	0.89	0.56	1.24	1.38	0.03	0.02	1.27	100	146	1.26	393	216	7.19	25.6	65.46	1.80	124	269	104	8.51
SHD-G3-02		89.2	4.42	0.97	0.91	0.61	0.94	0.96	0.14	0.02	2.21	100.3	113	1.16	364	197	6.64	15.6	60.57	1.77	139	234	82.1	7.23
SHD-G3-03		87.9	4.13	1.46	0.63	0.58	1.42	0.87	0.13	0.03	2.67	99.8	167	1.44	421	248	7.85	19.5	72.71	2.13	108	251	98.2	7.88
SHD-G3-04		85.1	6.72	1.38	0.76	0.79	0.99	1.14	0.18	0.02	2.93	99.9	125	1.32	389	209	7.02	13.7	68.29	1.78	122	245	87.2	6.94
SHD-G3-05		85.2	7.84	1.29	0.48	0.94	1.37	0.79	0.10	0.02	2.1	100.1	154	1.21	416	235	7.59	22.1	66.21	1.97	118	218	91.1	6.73
SHD-G4-01		61.3	8.22	19.11	2.33	2.09	1.23	0.93	0.54	0.03	4.63	100.4	264	2.09	724	318	6.32	18.1	55.58	2.23	167	287	71.2	4.39
SHD-G4-02		62.9	7.19	18.42	2.56	2.18	1.45	0.74	0.42	0.07	4.12	100	195	2.14	826	241	5.14	17.6	52.76	2.07	171	239	60.7	5.32
SHD-G4-03	G4	59.5	9.21	20.2	1.78	1.77	1.47	0.89	0.58	0.06	4.8	100.2	305	2.36	734	428	7.19	20.3	61.33	2.32	154	271	69.1	4.57
SHD-G4-04		61.2	8.52	18.73	2.64	2.67	2.19	0.68	0.46	0.04	3.28	100.4	232	1.87	699	297	6.99	15.9	58.99	2.19	165	254	79.3	6.13
SHD-G4-05		60.9	8.03	19.65	2.47	1.58	1.42	0.81	0.57	0.05	4.58	100	245	2.14	763	345	5.84	16.9	46.61	2.34	158	302	64.4	5.38
SHD-G5-01		56.7	13.3	16.11	2.61	1.91	1.57	1.21	0.42	0.12	6.44	100.4	211	1.96	957	284	8.21	21.4	80.34	3.31	175	361	105	7.94
SHD-G5-02		57.5	11.8	14.46	4.54	2.31	2.15	0.47	0.25	0.09	7.22	100.7	165	1.74	761	229	6.97	26.8	71.29	2.64	198	314	98.7	4.85
SHD-G5-03		55.9	12.5	15.32	3.78	2.81	1.83	0.83	0.56	0.08	6.73	100.3	245	2.47	1153	308	8.61	22.6	83.47	3.48	165	402	123	8.39
SHD-G5-04		56.8	12.3	14.94	3.49	1.56	2.90	0.92	0.23	0.08	7.08	100.3	196	1.89	846	268	7.44	17.8	78.37	2.83	185	345	85.9	7.61
SHD-G5-05		57.2	12.1	14.83	4.27	1.48	3.34	0.68	0.34	0.1	5.79	100.1	237	1.16	981	304	8.32	20.2	69.89	3.17	157	309	117	8.02
SHD-G6-01		63.7	13.7	6.54	3.14	2.68	1.87	1.23	0.56	0.01	7.11	100.5	70.2	0.78	204	168	4.96	11.5	62.7	1.17	211	421	68.9	6.01
SHD-G6-02		64.5	12.3	7.19	2.65	3.29	2.36	1.58	0.70	0.07	5.78	100.4	55.6	0.64	183	142	4.34	9.64	55.94	0.83	237	397	77.5	4.82
SHD-G6-03	G6	62.8	13.9	7.56	3.24	2.34	2.01	2.09	0.34	0.06	5.84	100.1	85.3	0.89	228	151	5.32	8.69	66.11	0.96	194	430	74.6	5.36
SHD-G6-04		64.1	15.4	6.32	2.28	2.44	2.13	2.14	0.72	0.03	4.96	100.5	65.4	0.73	216	176	5.61	13.5	68.12	1.14	215	384	64.03	4.97
SHD-G6-05		62.3	14.2	5.58	4.17	3.51	1.87	1.39	0.76	0.1	6.48	100.3	75.9	0.88	199	155	6.12	11.3	57.37	0.86	186	463	71.7	5.26
SHD-G7-01		52.3	6.84	12.63	13.6	2.43	0.86	0.74	0.34	0.09	10.5	100.3	383	3.11	1605	986	15	28.9	90.34	2.74	487	302	66.9	7.13
SHD-G7-02		48.3	8.57	11.24	15.2	3.74	1.34	0.83	0.32	0.11	10.4	100	416	3.24	1758	1328	17.9	31.2	100.3	3.76	542	347	84.7	5.89
SHD-G7-03		50.1	7.19	13.72	13	2.9	1.18	0.66	0.47	0.07	11.1	100.3	296	2.65	1384	728	12.6	26.5	84.57	3.44	610	296	79.5	6.47
SHD-G7-04		49.6	8.61	12.3	13.3	1.56	1.08	1.09	0.29	0.07	12.3	100.1	344	2.97	1499	889	14.3	25.3	88.65	3.37	515	251	73.6	4.63
SHD-G7-05		49.1	7.98	11.47	14.4	4.41	1.54	0.77	0.64	0.12	9.81	100.2	365	3.43	1587	942	15.2	32.2	80.34	3.59	647	328	75.3	6.08

G_5 (i.e., argillic with Fe-oxides or leached cap) major-element chemistry shows intermediate Al_2O_3–K_2O values within the argillic range, elevated Fe_2O_3, and moderate CaO contents (Table 1). Trace element patterns are characterized by elevated As and moderate Au–Cu concentrations, reflecting a transitional geochemical signature between the argillic (G_1) and oxide (G_4) domains. The combination of increased Fe_2O_3 and argillic-range Al_2O_3–K_2O values typifies oxidized argillic caps formed through partial leaching and supergene overprinting above mineralized structural corridors.

G_6 (i.e., propylitic zone; chlorite–epidote–calcite assemblage) major-element compositions display balanced Fe–Mg–Ca ratios and moderate Al_2O_3 contents, indicating limited hydrothermal leaching and minimal alkali depletion (Table 1). Trace element abundances remain near background levels, with Sr and Ba retention attributed to residual plagioclase and fine carbonate microveining. The near-background metal contents, coupled with Fe–Mg–Ca stability and subdued alteration signatures, confirm the distal, outer-halo character of G_6. These compositions provide a geochemical baseline and define vector gradients toward progressively more reactive, clay-, carbonate-, or Fe-oxide–rich alteration zones.

G_7 (i.e., carbonate + Fe-oxide mix; oxidized quartz–carbonate veins) major-element geochemistry is characterized by elevated CaO and MgO, significant Fe_2O_3, high LOI, and enrichment in Sr, all indicative of carbonate addition and oxidation (Table 1). Trace elements display the highest Au–Cu–As concentrations among all groups, reflecting vein-proximal oxidation processes and secondary malachite coatings. The combined CaO–MgO–Sr enrichment, elevated Fe_2O_3, and high LOI values confirm the presence of oxidized carbonate vein assemblages, whereas the pronounced Au–Cu–As maxima delineate feeder-proximal structural corridors. G_7 thus serves as a first-order geochemical indicator for prioritizing trenching and drilling along mineralized fault–vein zones.

4.3. Spectroscopy–Spectral Analysis

Spectroscopic analysis of the seven alteration–lithological groups reveals distinct absorption features that correlate with mineral assemblages confirmed by XRD and petrography. It should be noted that the spectral representation in Figure 8 varies by group. Groups G_1–G_3 display all six individual spectra to document intra-group variability, whereas groups G_4–G_7 are represented by median spectra due to smaller sample sizes (G_4, n = 1; G_5–G_7, n = 2–3) and the high spectral homogeneity within these groups. This strategy ensures that diagnostic absorption features are clearly conveyed without redundancy, while all spectral assignments are corroborated by independent XRD mineralogy and whole-rock geochemical analyses, confirming their robustness and reproducibility.

Group G_1 is spectrally defined by three key characteristics. First, an absorption feature at ~1.40 μm indicates the presence of structural and adsorbed hydroxyl groups in phyllosilicates (Figure 7a). Minor wavelength shifts (±0.01–0.02 μm) suggest variations in hydration state and crystallographic order, which is consistent with the presence of mixed-layer illitic or kaolinitic phases. Second, the ~1.90 μm H_2O combination band exhibits subtle depth variations, implying differences in interlayer water content. Samples derived from altered volcanic tuffs typically display deeper 1.90 μm minima than those from subvolcanic units, and this enhanced depth may indicate a supergene overprint. Third, a strong Al–OH absorption feature at ~2.20–2.21 μm is the most diagnostic for G_1, corresponding to Al–OH vibrations in illite and kaolinite; variations in its depth and shape reflect the relative abundance and crystallinity of these minerals. Critically, the absence of absorption shoulders in the 2.30–2.33 μm region indicates a lack of significant Mg- or Fe-bearing phyllosilicates such as chlorite or smectite. Furthermore, no notable absorptions are present in the 2.33–2.35 μm (carbonate) or 2.25–2.28 μm (Fe–OH) regions, which further supports the mineralogical homogeneity inferred from petrographic and

XRD data. Collectively, these spectral patterns are consistent with an argillic alteration signature and correspond to those documented in epithermal systems globally [3,11,39].

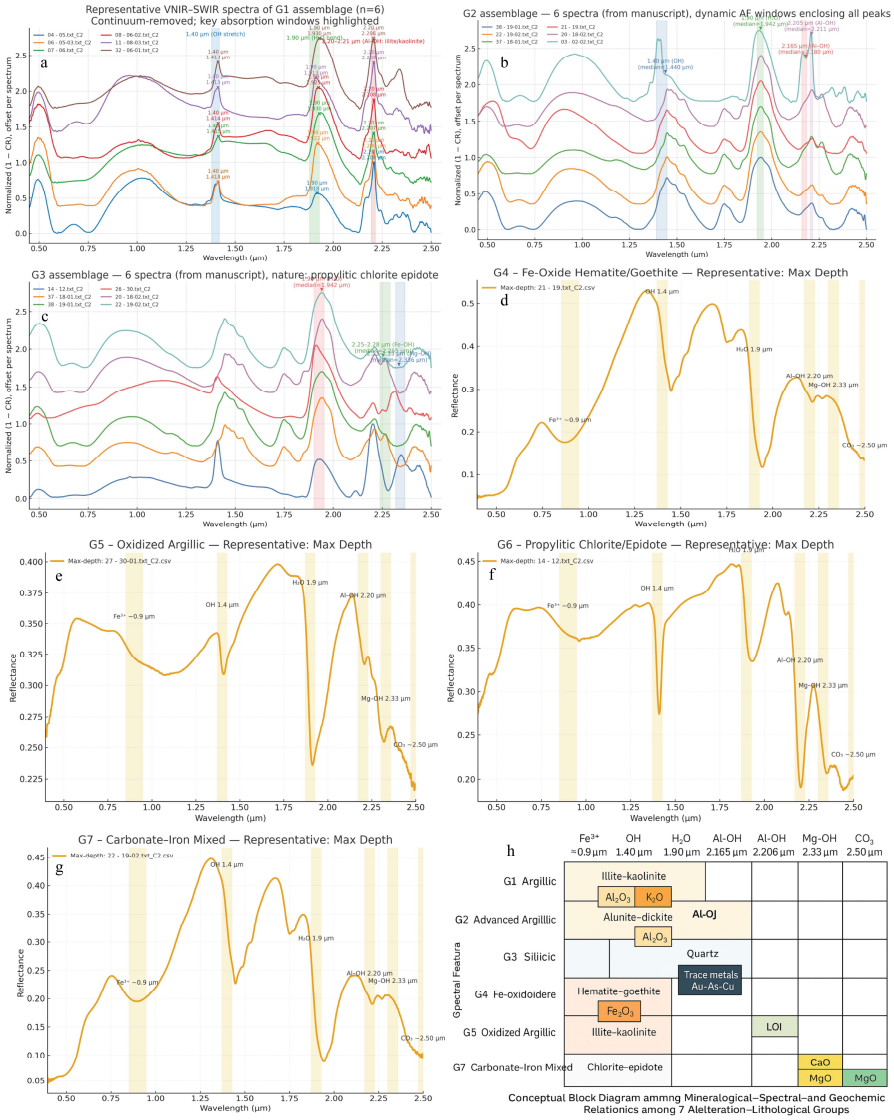


Figure 8. (**a**–**c**) VNIR–SWIR spectra of G_1–G_3 samples (n = 6) show key absorption features at ~1.40 μm (OH), ~1.90 μm (H_2O), and ~2.20–2.21 μm (Al–OH) for clay- and quartz-rich assemblages. (**d**) G_4 Fe-oxide spectrum exhibits broad Fe^{3+} (~0.9 μm) with OH/H_2O bands; minor Al–OH, weak Mg–OH, and faint CO_3 indicate supergene oxidation overprinting earlier hydrothermal minerals. (**e**) G_5 Oxidized argillic shows subtle–moderate Fe^{3+} (~0.9 μm), strong OH/H_2O, Al–OH (~2.20 μm), weak Mg–OH, and faint CO_3, reflecting supergene clay–oxide overprint. (**f**) G_6 Propylitic chlorite–epidote spectrum is dominated by Mg–OH (~2.33 μm) with subordinate Al–OH, OH, and H_2O; weak Fe^{3+} and CO_3 indicate minimal supergene influence. (**g**) G_7 carbonate–iron mixed spectrum shows prominent CO_3 (~2.50 μm), moderate Fe^{3+} (~0.9 μm), strong OH/H_2O, and weak Al–OH/Mg–OH, consistent with oxidized carbonate lithologies. (**h**) Conceptual matrix links VNIR–SWIR bands (Fe^{3+}, OH/H_2O, Al–OH, Mg–OH, and CO_3) to dominant minerals (illite–kaolinite, alunite–dickite, quartz, hematite–goethite, and chlorite–epidote) and geochemical trends (Al_2O_3, K_2O, Fe_2O_3, CaO, MgO, and LOI), illustrating the continuum from argillic to oxidized, silicified, carbonate-bearing, and propylitic domains in the Shadan hydrothermal system. Groups G_1–G_3 present the complete set of individual spectra (n = 6 each) to document intra-group variability in absorption feature geometry and depth. For groups G_4–G_7, representative median spectra are shown due to smaller sample sizes (G_4, n = 1; G_5–G_7, n = 2–3) and high intra-group spectral homogeneity. The spectral classifications for all groups are corroborated by independent XRD and whole-rock geochemical analyses, confirming the robustness of the assigned alteration facies.

Group G_2 is distinguished by three principal spectral features (Figure 7b). First, a strong and well-defined Al–OH absorption at ~2.165 μm, diagnostic of alunite and/or dickite, is present; this is often accompanied by a secondary, weaker Al–OH feature at ~2.205 μm, attributed to kaolinite or residual illite. The feature at ~2.165 μm is a key indicator of acidic conditions and high-temperature advanced argillic alteration, which is crucial for identifying high-sulfidation environments [9]. Second, pronounced OH and H_2O absorptions occur at ~1.40 μm (OH-stretch) and ~1.90 μm (H-O-H bend combination). Third, the absence of Mg–OH absorptions in the 2.30–2.35 μm region reflects the scarcity of chlorite and smectite phases. These spectral characteristics align closely with those in the USGS spectral library and are consistent with advanced argillic alteration in high- and intermediate-sulfidation systems worldwide [3,4,31,39]. Geochemically, these argillic to advanced argillic domains (G_1–G_2) correlate with elevated concentrations of Al and pathfinder elements (As and Sb), effectively marking the principal fluid pathways for the hydrothermal system.

Group G_3 exhibits diagnostic features that differ markedly from the clay-dominated signatures of G_1 and G_2 (Figure 7c). The principal absorption bands in the VNIR–SWIR region include: (1) moderate to strong Mg–OH and Fe–OH absorptions between 2.32 and 2.35 μm, consistent with chlorite and epidote; (2) variable Fe–OH absorption shoulders at ~2.25–2.28 μm, interpreted as localized epidote or jarosite overprints; (3) a H_2O combination band at ~1.90 μm, attributed to molecular water in phyllosilicates and other hydrous minerals; (4) weak to absent Al–OH bands, reflecting the lower abundance of illite and kaolinite compared to G_1 and G_2; and (5) occasional carbonate absorptions at ~2.48–2.52 μm, indicating the presence of calcite or dolomite. The co-occurrence of these Mg–OH/Fe–OH and carbonate features represents a definitive spectral signature of propylitic alteration and serves as a key vector towards the hydrothermal center in many systems [40]. These spectral attributes justify the classification of G_3 as a distinct group, which we interpret as a transitional alteration zone between the advanced argillic (G_2) and the deeper, more pervasive propylitic facies.

The representative spectrum for G_4 is dominated by a broad Fe^{3+} absorption feature at ~0.9 μm, characteristic of hematite and/or goethite (Figure 7d). This is accompanied by strong OH (~1.4 μm) and H_2O (~1.9 μm) absorptions, attributable to adsorbed water on iron-oxide surfaces and minor residual phyllosilicates. In contrast, SWIR features between 2.0 and 2.4 μm are subdued: a weak Al–OH shoulder at ~2.20 μm indicates minor residual illite/kaolinite; Mg–OH absorption at ~2.33 μm is absent; and a faint CO_3^{2-} overtone at ~2.50 μm suggests a minor carbonate overprint or accessory calcite/dolomite in fractures. This spectral suite—dominated by ferric iron with muted phyllosilicate and carbonate features—is a recognized fingerprint of gossanous caps in VNIR-SWIR studies and is diagnostic of supergene oxidation overprinting earlier hydrothermal assemblages. Although G_4 is currently represented by a single spectrum, its band geometry aligns with supergene Fe-oxide facies reported in epithermal districts. In contrast to the clay-dominated groups G_1–G_2, G_4 lacks the strong Al–OH features between 2.16–2.21 μm and exhibits significantly weaker overall hydration. Furthermore, unlike the propylitic G_3 group, it shows no evidence of the Mg–Fe–OH signature from chlorite/epidote at ~2.32–2.35 μm. The spectral dominance of Fe^{3+} at ~0.9 μm, coupled with weak Al–OH and absent Mg–OH features, therefore confirms the interpretation of G_4 as an oxidation cap, distinct from the primary hydrothermal alteration zones.

Group G_5 displays a composite spectral signature indicative of a leached or oxidized argillic cap (Figure 7e). The representative spectrum is characterized by: (1) a Fe^{3+} absorption feature at ~0.9 μm that is present but subtler than in the gossanous G_4, indicating moderate ferric iron development without a fully expressed oxide cap; (2) well-developed

OH (~1.4 μm) and H_2O (~1.9 μm) absorptions, reflecting bound water in clays and microporosity typical of weathered argillic facies; (3) a clear Al–OH feature at ~2.20 μm, indicative of illite and/or kaolinite, which is generally shallower (mean depth: 0.043) than in G_1, consistent with clay dilution by iron oxides and textural disruption; (4) a weak Mg–OH absorption at ~2.33 μm (mean depth: 0.013), indicating only a minor chlorite/smectite component and distinguishing it from the propylitic signature of G_3; and (5) a faint CO_3^{2-} absorption at ~2.50 μm (mean depth: 0.026), suggesting scarce accessory calcite or dolomite as late veinlets or weathering products. This signature, featuring both Fe-oxide and well-developed clay absorptions, is characteristic of a leached argillic cap where hypogene clay minerals persist but are pervasively stained by iron oxides [40,41]. Spatially, these oxidized facies (G_4–G_5) typically cap or flank the higher-grade argillic and propylitic zones, recording the extent of supergene processes.

The representative spectrum of G_6 is diagnostic of a propylitic alteration assemblage (Figure 7f), characterized by: (1) a defining Mg–OH absorption feature at ~2.33 μm, consistent with chlorite and/or epidote; (2) a subordinate Al–OH feature at ~2.20 μm (mean depth: 0.301), reflecting a minor component of illite/sericite; (3) pronounced OH (~1.4 μm) and H_2O (~1.9 μm) features corresponding to structural water and hydroxyl groups in chlorite and epidote; (4) a weak Fe^{3+} feature at ~0.9 μm (mean depth: 0.008), indicating limited oxidation and the lack of a significant supergene overprint as seen in G_4–G_5; and (5) the absence of a CO_3^{2-} absorption at ~2.50 μm (mean depth: 0.001), indicating negligible calcite, dolomite, or late carbonate veining. These characteristics align with classical propylitic spectral patterns [3,4,11]. The consistent strength and position of the Mg–OH feature in G_6 provide a key parameter for systematically mapping the distal propylitic halo and its chemical gradients in porphyry–epithermal environments. We interpret these G_6 spectra to represent the distal or deeper propylitic halo, where Mg-Fe silicates stable at higher pH and lower acidity. Consequently, the strength of the Mg–OH feature serves as a robust distal vector.

The representative spectrum of G_7 (Figure 7g) displays the defining combination of Fe-oxide and carbonate absorption features: (1) a well-expressed CO_3^{2-} absorption at ~2.50 μm (mean depth: 0.095) indicates the presence of persistent calcite/dolomite, likely as a cement; (2) a Fe^{3+} absorption feature at ~0.9 μm (mean depth: 0.039) reflects hematite/goethite development under near-surface oxidative conditions; (3) prominent OH (~1.4 μm) and H_2O (~1.9 μm) bands are consistent with superficial hydration, porosity, and minor clay residues; (4) a very weak Al–OH feature at ~2.20 μm (mean depth: 0.067) indicates only limited residual illite/kaolinite or minor mixing with argillic layers; and (5) an absent Mg–OH absorption at ~2.33 μm (mean depth: 0.001) distinguishes G_7 from the propylitic chlorite-epidote assemblages (G_3 and G_6) and confirms minimal Mg-silicate involvement. These spectral signatures confirm a carbonate-rich substrate experiencing supergene ferric overprinting, rather than primary hydrothermal carbonate alteration or clay-dominated assemblages. The carbonate–iron mixed zones (G_7) indicate carbonate persistence with oxidative fronts, potentially outlining permeability contrasts.

Our findings demonstrate that each alteration group is defined by a distinct spectral fingerprint: G_1 and G_2 by strong Al–OH features (illite–smectite–kaolinite and alunite–dickite); G_4 and G_5 by prominent Fe^{3+} absorption (hematite–goethite); G_6 by strong Mg–OH absorption (chlorite–epidote); G_7 by elevated CO_3 bands (carbonate–iron oxide); and G_3 by a minimal spectral response resulting from pervasive silicification.

4.4. Subtle Variations, Overlapping Absorption Features, and Geochemical Control (New)

Diagnostic VNIR–SWIR absorption features reflect the presence and relative abundance of specific mineral phases and are systematically influenced by bulk geochemical

composition and fluid–rock interaction conditions. Variations in band position, depth, and shape across the seven alteration–lithological groups are controlled by differences in mineral assemblages (e.g., clays, Fe-oxides, chlorite–epidote, and carbonates) and associated chemical drivers such as Al_2O_3, Fe_2O_3, MgO, CaO, and LOI. Conceptual synthesis figures integrate these spectral, mineralogical, and geochemical relationships and provide a framework for interpreting alteration processes within the Shadan hydrothermal system. Although several alteration groups occupy overlapping diagnostic VNIR–SWIR spectral windows, subtle variations in peak positions (PPs), absorption feature (AF) depths, and band geometries enable reliable discrimination among groups and provide insight into fluid chemistry, redox state, and mineral crystallinity. These relationships are summarized in Table 2, which links key absorption features to controlling mineral phases, dominant geochemical drivers, and their semiquantitative correlation strengths across the seven alteration–lithological groups. Collectively, these correlations illustrate how spectral responses consistently track mineralogical and geochemical variations within the Shadan hydrothermal system.

Table 2. Absorption features, mineralogical controls, dominant chemical drivers, and estimated correlation strength.

AF/PP Window	Controlling Minerals	Key Chemical Drivers	Most Affected Groups	Estimated Correlation Strength
~2.165 μm (PP)	Alunite, dickite	High Al_2O_3, sulfate activity, low pH	G2 > G5	85–90%
~2.20 μm (PP/AF)	Illite, kaolinite	High Al_2O_3, K metasomatism, feldspar breakdown	G1 > G5 > G7	80–85%
~2.33 μm (AF)	Chlorite, epidote	High MgO, FeO–Fe_2O_3, CaO±; neutral–slightly basic fluids	G6 > G3	75–85%
~0.90 μm (AF)	Hematite, goethite	Fe^{3+} enrichment; oxidation intensity	G4 > G7 > G5	70–80%
~2.50 μm (AF/PP)	Calcite, dolomite	CaO, CO_2; carbonate abundance/replacement	G7 > G3	70–80%
1.40 & 1.90 μm (AF)	Hydrous phases	Hydration state, porosity, micro-porosity	G1–G2–G5–G6–G7	50–60%
2.25–2.28 μm (shoulder)	Epidote/Fe–clays (minor)	Fe–Ca–Mg mixing; oxidation	G3 (minor), G6, G7	50–55%

The systematic correspondence between diagnostic absorption features, mineral assemblages, and compositional trends is synthesized in a conceptual framework that integrates spectral, mineralogical, and geochemical datasets (Figure 7). This framework highlights the continuum from clay-dominated argillic assemblages to oxidized, silicified, carbonate-bearing, and propylitic domains, and demonstrates how specific VNIR–SWIR bands respond to dominant mineral phases and chemical drivers.

(i) Al–OH domain (2.165–2.20 μm): G_1 and G_2 both display prominent Al–OH absorptions; however, G_1 exhibits a maximum near 2.20 μm (illite–kaolinite association), whereas G_2 is distinctly shifted toward ~2.165 μm (alunite–dickite composition). The shorter wavelength of G_2 reflects elevated Al activity, increased sulfate content, and a lower pH regime, characteristic of advanced argillic alteration. G_5 partially overlaps G_1 but exhibits a shallower 2.20 μm absorption and an additional Fe^{3+} feature near 0.9 μm, indicative of an oxidative overprint rather than a purely clay-dominated signature. Subtle broadening and

left-shoulder asymmetry around 2.20 µm in G_5 suggest mixed clay–oxide microtextures (Figure 7). (ii) Mg–OH domain (2.31–2.36 µm): Both G_6 and G_3 display Mg–OH absorptions; however, G_6 shows a sharper and deeper trough near 2.33 µm (chlorite–epidote assemblage), whereas G_3 is characterized by shallower depths, broader curvature, and locally weak CO_3 shoulders, signifying a transitional intermediate-to-propylitic environment with mixed mineral phases. The relative absorption depth hierarchy ($G_6 > G_3$) delineates purer propylitic conditions and higher-temperature, near-neutral pH fluids within G_6 (Figures 7 and 8). (iii) Fe^{3+} domain (~0.9 µm): Among G_4, G_7, and G_5, G_4 exhibits the most intense and broad Fe^{3+} absorption (hematite–goethite dominance), G_7 displays moderate intensity (oxide–carbonate assemblage), and G5 shows weaker absorption consistent with an oxide overprint on clays. This spectral gradient reflects progressive oxidation intensity and varying host-rock mineralogy. The co-occurrence of CO_3 in G_7 indicates oxidized, carbonate-bearing lithologies, whereas G_4 represents a supergene oxide cap with minimal clay or carbonate spectral signatures (Figures 9 and 10). (iv) CO_3 domain (~2.50 µm): G_7 displays the most prominent CO_3 absorption, frequently coupled with Fe^{3+} features, whereas G_3 exhibits only localized or weak CO_3 absorptions associated with carbonate replacement zones or veins. These contrasts reflect greater carbonate persistence and vein abundance in G_7 compared to the mixed propylitic mineralogy in G_3 (Figure 10). (v) Hydration bands (1.40 and 1.90 µm): Hydrous overtone absorptions are pervasive across all alteration groups, producing broadly similar band morphologies; however, variations in absorption depth correspond to differences in grain size, porosity, interlayer or bound water, and supergene modification, yielding only moderate geochemical correlation (Tables 2 and 3; Figure 9).

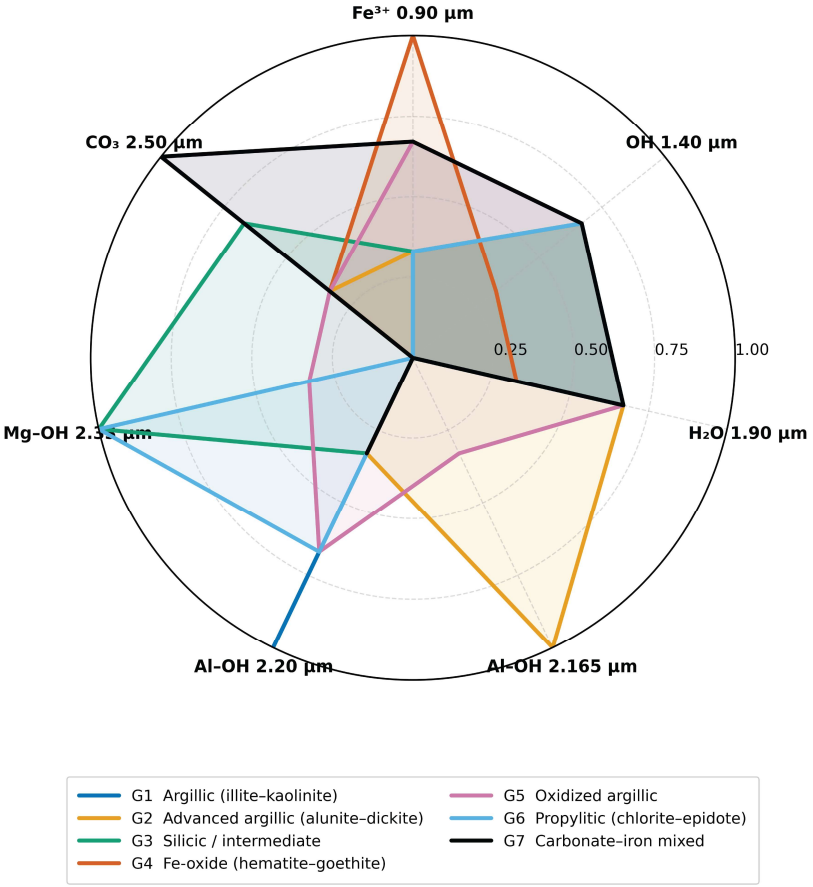


Figure 9. Radar plot comparing diagnostic absorption band intensities (~0.9, 1.40, 1.90, 2.165, 2.20, 2.33, and 2.50 µm) across the seven spectral–lithological groups (G_1–G_7). The plot highlights spectral contrasts reflecting dominant minerals: Al–OH clays (G_1–G_2), Fe-oxides (G_4–G_5), Mg–Fe silicates (G_6), and carbonates (G_7), with G_3 representing a feature-poor, quartz-rich silicic endmember.

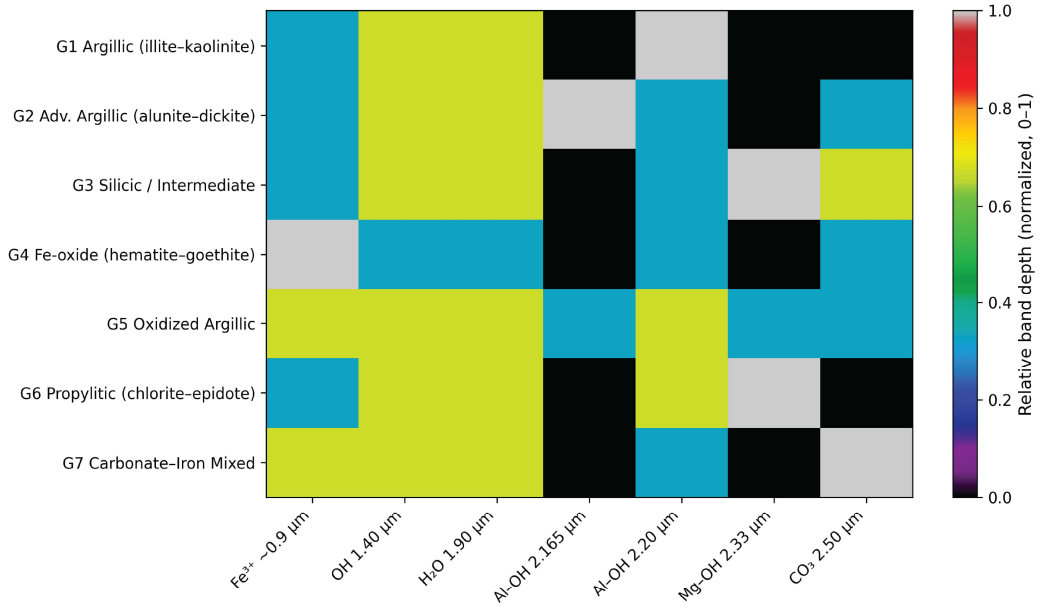


Figure 10. Heatmap showing relative absorption strengths (0–1) at key wavelengths (Fe^{3+} ~0.9 µm, OH 1.40 µm, H_2O 1.90 µm, Al–OH 2.165 and 2.20 µm, Mg–OH 2.33 µm, CO_3 2.50 µm) for the seven spectral–lithological groups (G_1–G_7). The matrix highlights characteristic spectral signatures of dominant minerals (e.g., clays, carbonates, Fe-oxides, and chlorite–epidote) and enables semi-quantitative comparison of absorption intensities across alteration domains.

Table 3. Summary of spectral–mineralogical–geochemical relationships by spectral group (qualitative).

Group	Dominant Minerals	Key Spectral Bands	Geochemical Traits	Process Interpretation
G_1	Illite, kaolinite	Al–OH ~2.20; OH 1.4; H_2O 1.9	High Al_2O_3; Ca–Mg–low Na	Argillic (proximal)
G_2	Alunite, kaolinite/dickite	Al–OH ~2.165; OH/H_2O strong	High Al_2O_3; low alkalis; sulfate-rich	Advanced argillic (acidic)
G_3	Chlorite, epidote ± carbonate	Mg–Fe–OH ~2.32–2.35; CO_3 variable	High Fe–Mg; lower alkalis	Silicic/intermediate–propylitic
G_4	Hematite, goethite	Fe^{3+} ~0.9; OH/H_2O subdued	High Fe-oxide; low clays	Supergene oxidation cap
G_5	Illite/Kaolinite + Fe-oxides	Al–OH ~2.20 + Fe^{3+} ~0.9	Mixed; low alkalis; high Fe-oxide	Oxidized argillic (supergene clay–oxide)
G_6	Chlorite, epidote	Mg–OH ~2.33; OH/H_2O present	High Fe–Mg; moderate Ca	Propylitic (distal)
G_7	Calcite/Dolomite + Fe-oxides	CO_3 ~2.50 + Fe^{3+} ~0.9	Ca–CO_2 persists; high Fe-oxide	Carbonate–iron mixed (supergene)

The integrated relationships among spectral absorption features, mineral assemblages, and geochemical drivers are further conceptualized in a tri-layer linkage model (Figure 11). This model illustrates how diagnostic VNIR–SWIR bands translate into specific mineralogical assemblages and are reflected in bulk compositional parameters such as Al_2O_3/K_2O, Fe_2O_3, CaO/MgO, LOI, and associated trace metals. Together, Figures 8–10 provide a unified interpretation that links field mineralogy, spectral responses, and geochemical trends, reinforcing the robustness of the spectral–lithological classification applied to the Shadan hydrothermal system.

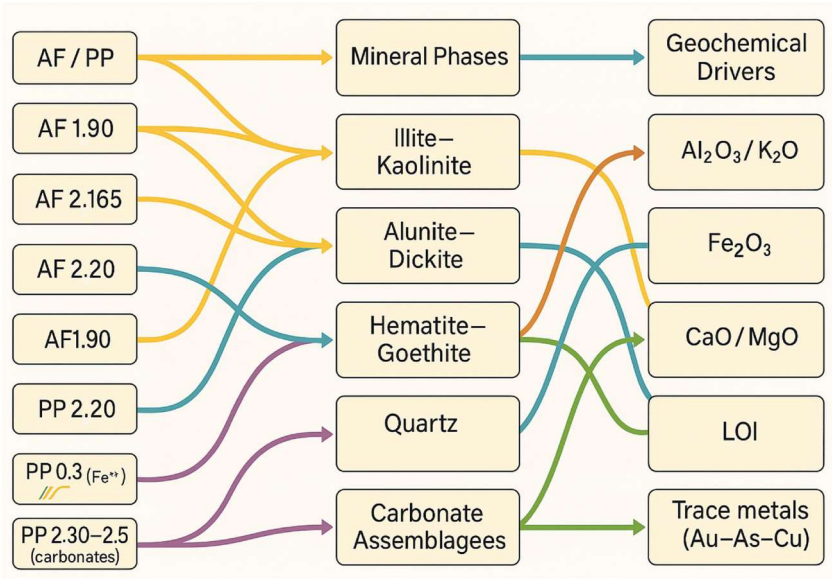


Figure 11. Tri-layer conceptual block diagram linking spectral absorption features (AF/PP metrics), dominant minerals, and geochemical drivers. Colored pathways illustrate how specific bands (Al–OH, Fe^{3+}, Mg–OH, and CO_3) correspond to mineral assemblages (e.g., illite–kaolinite, alunite–dickite, hematite–goethite, carbonates) and are reflected in compositional parameters across spectral–lithological groups G_1–G_7.

5. Conclusions

1. Integrated VNIR–SWIR spectroscopy, XRD mineralogy, and whole-rock geochemistry define seven alteration–lithological groups (G_1–G_7) forming a continuous gradient from deep propylitic to shallow argillic, oxidized, and carbonate-bearing domains in the Shadan Au–Cu system.
2. The vertical and lateral zonation defines a systematic mineralogical progression from quartz–illite–kaolinite–dominated central assemblages to peripheral chlorite–epidote halos and late-stage carbonate–Fe vein networks. This spatial architecture records progressive thermal decline and coupled evolution of fluid pH and redox conditions during multistage hydrothermal circulation, consistent with telescoping in a porphyry–epithermal system driven by uplift and structural reactivation.
3. Diagnostic absorptions (~0.9, 2.20, 2.33, 2.50 μm) correlate with XRD-verified mineral assemblages and major-element systematics; band shifts in Al–OH and Mg–OH record octahedral Al–Mg–Fe substitution and temperature-dependent phyllosilicate evolution.
4. Fe^{3+} and CO_3 features document supergene oxidation and late carbonate veining, marking fluid evolution from magmatic–hydrothermal to mixed meteoric–hydrothermal regimes.
5. Au–Cu enrichment spatially associated with mixed argillic–carbonate and oxide assemblages indicates structurally focused, redox-controlled ore deposition governed by permeability and fluid mixing.
6. The integrated spectral–mineralogical–geochemical model provides a transferable framework for alteration mapping and vectoring toward mineralized centers in post-collisional porphyry–epithermal systems.

Supplementary Materials: The following supporting information can be downloaded at: https://www.mdpi.com/article/10.3390/min16040379/s1, Table S1: Representative whole rock major and trace element compositions of Shadan region.

Author Contributions: Conceptualization, D.R., H.F. and S.B.; methodology, N.N., H.F. and S.B.; software, H.F. and S.B.; validation, H.F. and S.B.; formal analysis, D.R., N.N., S.B., H.F. and S.M.; investigation, D.R., N.N., S.B., H.F. and S.M.; resources, D.R., N.N., S.B., H.F. and S.M.; data curation, D.R., H.F. and S.B.; writing—original draft preparation, H.F. and S.B.; writing—review and editing, H.F., S.B., D.R. and N.N.; visualization, H.F., S.B. and D.R.; supervision, S.B.; project administration, S.B. and D.R.; funding acquisition, S.B. and D.R. All authors have read and agreed to the published version of the manuscript.

Funding: This research received no external funding.

Data Availability Statement: The original contributions presented in this study are included in the article/Supplementary Materials. Further inquiries can be directed to the corresponding author.

Acknowledgments: The authors acknowledge Karand Sadr Jahan Mines and Mineral Industries Co., for providing access to technical datasets and for granting permission to use and adapt field and mapping data for scientific publication.

Conflicts of Interest: Davood Raeisi and Shahrouz Babazadeh are employees of Karand Sadr Jahan Mines and Mineral Industries Co., The paper reflects the views of the scientists and not the company.

Appendix A

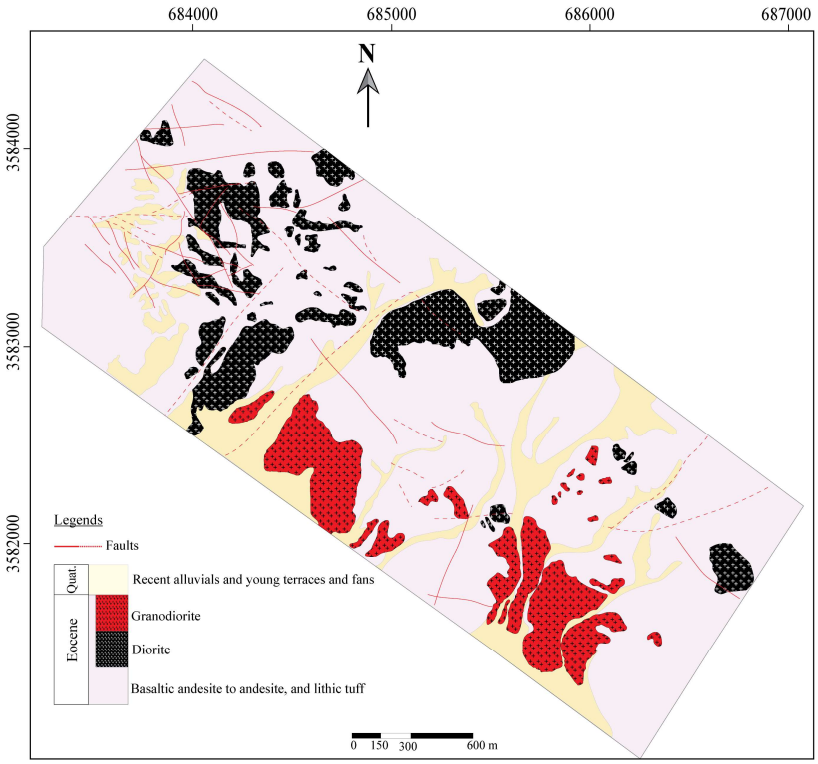


Figure A1. Geological maps of the Shadan region showing lithological units.

References

1. Hunt, G.R. Spectral signatures of minerals in the visible and near-infrared. *Geophysics* **1977**, *42*, 468–671. [CrossRef]
2. Clark, R.N.; Swayze, G.A.; Gallagher, A.J.; King, T.V.V.; Calvin, W.M. High spectral-resolution reflectance spectroscopy of minerals. *J. Geophys. Res.* **1990**, *95*, 12653–12680. [CrossRef]
3. Clark, R.N.; Swayze, G.A.; Livo, K.E.; Kokaly, R.F.; Sutley, S.J.; Dalton, J.B.; McDougal, R.R.; Gent, C.A. Imaging spectroscopy: Earth and planetary remote sensing with the USGS Tetracorder and expert systems. *J. Geophys. Res. Planets* **2003**, *108*, 5131. [CrossRef]

4. Kokaly, R.F.; Clark, R.N.; Swayze, G.A.; Livo, E.; Hoefen, T.; Pearson, N.; Wise, R.; Benzel, W.; Lowers, H.; Driscoll, R.; et al. *USGS Spectral Library Version 7*; USGS Crustal Geophysics and Geochemistry Science Center: Denver, CO, USA, 2017; Volume 1035. [CrossRef]
5. Koerting, S.; Koellner, T.; Müller, M.; Hinz, S.; Buchen, T.; Wenzel, V. A solar optical hyperspectral library of rare earth-bearing minerals. *Earth Syst. Sci. Data* **2019**, *11*, 637–660. [CrossRef]
6. Koerting, F.; Asadzadeh, S.; Hildebrand, J.C.; Savinova, E.; Kouzeli, E.; Nikolakopoulos, K.; Lindblom, D.; Koellner, N.; Buckley, S.J.; Lehman, M.; et al. VNIR–SWIR imaging spectroscopy for mining: Insights for hyperspectral drone applications. *Mining* **2024**, *4*, 1013–1057. [CrossRef]
7. Rowan, L.C.; Hook, S.J.; Abrams, M.J.; Mars, J.C. Mapping hydrothermally altered rocks at Cuprite, Nevada using Advanced Spaceborne Thermal Emission and Reflection Radiometer (ASTER), a new satellite imaging system. *Econ. Geol.* **2003**, *98*, 1019–1027. [CrossRef]
8. Mars, J.C.; Rowan, L.C. Regional mapping of phyllic- and argillic-altered rocks in the Zagros magmatic arc, Iran, using Advanced Spaceborne Thermal Emission and Reflection Radiometer (ASTER) data and logical-operator algorithms. *Geosphere* **2006**, *2*, 161–186. [CrossRef]
9. Bishop, J.L.; Lane, M.D.; Dyar, M.D.; Brown, A.J. Reflectance and emission spectroscopy study of four groups of phyllosilicates: Smectites, kaolinite-serpentines, chlorites and micas. *Clays Miner.* **2008**, *43*, 35–54. [CrossRef]
10. Kruse, F.A. Mapping surface mineralogy using imaging spectrometry. *Geomorphology* **2012**, *137*, 41–56. [CrossRef]
11. van der Meer, F.D.; van der Werff, H.M.A.; van Ruitenbeek, F.J.A.; Hecker, C.; Bakker, W.H.; Noomen, M.F.; van der Meijde, M.; Carranza, E.J.M.; de Smeth, J.B.; Woldai, T. Multi- and hyperspectral geologic remote sensing: A review. *Int. J. Appl. Earth Obs. Geoinf.* **2012**, *14*, 112–128. [CrossRef]
12. Chirico, R.; Mondillo, N.; Laukamp, C.; Mormone, A.; Di Martire, D.; Novellino, A.; Balassone, G. Mapping hydrothermal and supergene alteration zones associated with carbonate-hosted Zn–Pb deposits by using PRISMA satellite imagery supported by field-based hyperspectral data, mineralogical and geochemical analysis. *Ore Geol. Rev.* **2023**, *152*, 105244. [CrossRef]
13. Swayze, G.A.; Clark, R.N.; Goetz, A.F.H.; Livo, K.E.; Kruse, F.A.; Sutley, S.J.; Gallagher, A.J.; King, T.V.V. Mapping advanced argillic alteration at Cuprite, Nevada, using imaging spectroscopy. *Econ. Geol.* **2014**, *109*, 1179–1221. [CrossRef]
14. Agrawal, N.; Govil, H.; Chatterjee, S.; Mishra, G.; Mukherjee, S. Evaluation of machine learning techniques with AVIRIS-NG dataset in the identification and mapping of minerals. *Adv. Space Res.* **2022**, *73*, 1517–1533. [CrossRef]
15. Géring, L.; Kirsch, M.; Thiele, S.; De Lima Ribeiro, A.; Gloaguen, R.; Gutzmer, J. Spectral characterisation of hydrothermal alteration associated with sediment-hosted Cu–Ag mineralisation in the Central European Kupferschiefer. *Solid Earth* **2023**, *14*, 463–484. [CrossRef]
16. Asadzadeh, S.; Zhou, X.; Chabrillat, S. Assessment of the spaceborne EnMAP hyperspectral data for alteration mineral mapping: A case study of the Reko Diq porphyry Cu–Au deposit, Pakistan. *Remote Sens. Environ.* **2024**, *314*, 114389. [CrossRef]
17. Esmaeili, M.; Fathianpour, N.; Soltani-Mohammadi, S. PRISMA hyperspectral imagery for mapping alteration zones associated with Kuhpanj porphyry copper deposit, Southern Iran. *Eur. J. Remote Sens.* **2024**, *57*, 2299369. [CrossRef]
18. Sorrentino, A.; Chirico, R.; Corrado, F.; Laukamp, C.; Di Martire, D.; Mondillo, N. The application of PRISMA hyperspectral satellite imagery in the delineation of distinct hydrothermal alteration zones in the Chilean Andes: The Marimaca IOCG and the Río Blanco–Los Bronces Cu–Mo porphyry districts. *Ore Geol. Rev.* **2024**, *167*, 105998. [CrossRef]
19. Dell'Aversana, P. An integrated deep learning framework for classification of mineral thin sections and other geo-data, a tutorial. *Minerals* **2023**, *13*, 584. [CrossRef]
20. Tirrul, R.; Bell, I.R.; Griffis, R.J.; Camp, V.E. The Sistan suture zone of eastern Iran. *Geol. Soc. Am. Bull.* **1983**, *94*, 134–150. [CrossRef]
21. Bröcker, M.; Hövelkröger, Y.; Fotoohi Rad, G.; Berndt, J.; Scherer, E.E.; Kurzawa, T.; Moslempour, M.E. The magmatic and tectono-metamorphic history of the Sistan suture zone, Iran: New insights into a key region for the convergence between the Lut and Afghan blocks. *J. Asian Earth Sci.* **2022**, *236*, 105313. [CrossRef]
22. Walker, R.; Jackson, J. Offset and evolution of the Gowk fault, S.E. Iran: A major intra-continental strike-slip system. *J. Struct. Geol.* **2002**, *24*, 1677–1698. [CrossRef]
23. Raeisi, D.; Babazadeh, S.; Santosh, M.; Zhao, M.; Chiaradia, M.; Moghadam, H.S.; Choi, S.H.; Modabberi, S. Cenozoic flare-up in the Eastern Iran Magmatic Belt: The dynamic link between closure of the Neotethyan Ocean and mineralization in the Lut Block. *Int. Geol. Rev.* **2026**, *68*, 109–136. [CrossRef]
24. Clark, R.N.; Roush, T.L. Reflectance spectroscopy: Quantitative analysis techniques for minerals. *J. Geophys. Res.* **1984**, *89*, 6329–6340. [CrossRef]
25. Sillitoe, R.H. Porphyry copper systems. *Econ. Geol.* **2010**, *105*, 3–41. [CrossRef]
26. Thompson, A.J.B.; Hauff, P.L.; Robitaille, A.J. Alteration mapping in exploration: Application of short-wave infrared (SWIR) spectroscopy. *SEG Newsl.* **1999**, *39*, 16–27. [CrossRef]

27. Chang, Z.; Hedenquist, J.W.; White, N.C.; Cooke, D.R.; Roach, M.; Deyell, C.L.; Garcia, J.; Gemmell, J.B.; McKnight, S.; Cuison, A.L. Exploration tools for linked porphyry and epithermal deposits: Example from the Mankayan intrusion-centered Cu–Au district, Luzon, Philippines. *Econ. Geol.* **2011**, *106*, 1365–1398. [CrossRef]
28. Hedenquist, J.W.; Lowenstern, J.B. The role of magmas in the formation of hydrothermal ore deposits. *Nature* **1994**, *370*, 519–527. [CrossRef]
29. Sillitoe, R.H. Gold-rich porphyry deposits: Descriptive and genetic models and their role in exploration and discovery. In *Gold in 2000*; Hagemann, S.G., Brown, P.E., Eds.; Society of Economic Geologists: Littleton, CO, USA, 2000; Volume 13, pp. 315–345. [CrossRef]
30. Babazadeh, S.; Ghalamghash, J.; D'Antonio, M.; Furman, T. Hydrothermal alteration in Eshtehard volcanoes, Iran: Constraints from trace elements redistribution and stable isotope geochemistry. *J. Geochem. Explor.* **2021**, *222*, 106719. [CrossRef]
31. Raeisi, D.; Hajsadeghi, S.; Hosseinzadehsabeti, E.; Babazadeh, S.; Lentz, D.R.; Santosh, M. Exploration targeting in the Shadan porphyry gold–copper deposit, Lut Block, Iran: Analysis of spatial distribution of sheeted veins and lithogeochemical data. *Minerals* **2023**, *13*, 471. [CrossRef]
32. Dalm, M.; Buxton, M.W.N.; van Ruitenbeek, F.J.A. Discriminating ore and waste in a porphyry copper deposit using short-wavelength infrared (SWIR) hyperspectral imagery. *Miner. Eng.* **2017**, *105*, 10–18. [CrossRef]
33. Seedorff, E.; Dilles, J.H.; Proffett, J.M.; Einaudi, M.T.; Zurcher, L.; Stavast, W.J.A.; Johnson, D.A.; Barton, M.D. Porphyry deposits: Characteristics and origin of hypogene features. In *Economic Geology 100th Anniversary Volume, 1905–2005*; Lieber, S., Ed.; Society of Economic Geologists: Littleton, CO, USA, 2005; pp. 251–298. [CrossRef]
34. Simmons, S.F.; White, N.C.; John, D.A. Geological characteristics of epithermal precious and base-metal deposits. In *100th Anniversary Volume: Geology, Discovery, and Production of Epithermal and Porphyry Copper Deposits*; Hedenquist, J.W., Thompson, J.F.H., Goldfarb, R.J., Richards, J.P., Eds.; Society of Economic Geologists: Littleton, CO, USA, 2005; pp. 485–522. [CrossRef]
35. Huston, D.L.; Relvas, J.M.R.S.; Gemmell, J.B.; Drieberg, S. The role of granites in volcanic-hosted massive sulphide ore-forming systems: An assessment of magmatic-hydrothermal contributions. *Miner. Depos.* **2011**, *46*, 473–507. [CrossRef]
36. Sillitoe, R.H.; Hedenquist, J.W. Are alkalic porphyry deposits overlain by advanced argillic lithocaps? *Econ. Geol.* **2025**, *120*. [CrossRef]
37. Reed, M.H. Sulfide mineral precipitation from hydrothermal fluids. *Rev. Mineral. Geochem.* **2006**, *61*, 609–631. [CrossRef]
38. Sillitoe, R.H. Supergene, oxidized and enriched porphyry-copper and related deposits. In *100th Anniversary Volume: Geology, Discovery, and Production of Porphyry Copper Deposits*; Hedenquist, J.W., Thompson, J.F.H., Goldfarb, R.J., Richards, J.P., Eds.; Society of Economic Geologists: Littleton, CO, USA, 2005; pp. 723–751. [CrossRef]
39. Bedini, E. Application of WorldView-3 imagery and ASTER TIR data to map alteration minerals associated with the Rodalquilar gold deposits, southeast Spain. *Adv. Space Res.* **2019**, *63*, 3346–3357. [CrossRef]
40. Chen, L.; Sui, X.; Liu, R.; Chen, H.; Li, Y.; Zhang, X.; Chen, H. Mapping alteration minerals using ZY-1 02D hyperspectral remote sensing data in coalbed methane enrichment areas. *Remote Sens.* **2023**, *15*, 3590. [CrossRef]
41. Gholipour, B.; Omran, N.R.; Rabiee, A.; Mokhtari, M.A.A.; Babazadeh, S. ASTER-based alteration mapping and structural analysis of the Saheb Divan hydrothermal system, NW Iran: Implications for exploration programs. *Remote Sens. Appl. Soc. Environ.* **2025**, *38*, 101532. [CrossRef]

Disclaimer/Publisher's Note: The statements, opinions and data contained in all publications are solely those of the individual author(s) and contributor(s) and not of MDPI and/or the editor(s). MDPI and/or the editor(s) disclaim responsibility for any injury to people or property resulting from any ideas, methods, instructions or products referred to in the content.